



**HAL**  
open science

## The detection of intergalactic H $\alpha$ emission from the Slug Nebula at $z \sim 2.3$

Camille N. Leibler, Sebastiano Cantalupo, Bradford P. Holden, Piero Madau

► **To cite this version:**

Camille N. Leibler, Sebastiano Cantalupo, Bradford P. Holden, Piero Madau. The detection of intergalactic H  $\alpha$  emission from the Slug Nebula at  $z \sim 2.3$ . Monthly Notices of the Royal Astronomical Society, 2018, 480, pp.2094-2108. 10.1093/mnras/sty1764 . insu-03747913

**HAL Id: insu-03747913**

**<https://insu.hal.science/insu-03747913>**

Submitted on 9 Aug 2022

**HAL** is a multi-disciplinary open access archive for the deposit and dissemination of scientific research documents, whether they are published or not. The documents may come from teaching and research institutions in France or abroad, or from public or private research centers.

L'archive ouverte pluridisciplinaire **HAL**, est destinée au dépôt et à la diffusion de documents scientifiques de niveau recherche, publiés ou non, émanant des établissements d'enseignement et de recherche français ou étrangers, des laboratoires publics ou privés.

# The detection of intergalactic H $\alpha$ emission from the Slug Nebula at $z \sim 2.3$

Camille N. Leibler,<sup>1</sup> Sebastiano Cantalupo,<sup>2</sup> Bradford P. Holden<sup>1</sup> and Piero Madau<sup>1,3</sup>

<sup>1</sup>Department of Astronomy and Astrophysics, University of California Santa Cruz, 1156 High Street, Santa Cruz, CA 95064, USA

<sup>2</sup>Department of Physics, ETH Zurich, Wolfgang-Pauli-Strasse 27, 8093, Zurich, Switzerland

<sup>3</sup>Institut d'Astrophysique de Paris, Sorbonne Universités, UPMC Univ Paris 6 et CNRS, UMR 7095, 98 bis bd Arago, 75014 Paris, France

Accepted 2018 June 30. Received 2018 June 29; in original form 2017 October 5

## ABSTRACT

The Slug Nebula is one of the largest and most luminous Lyman- $\alpha$  (Ly $\alpha$ ) nebulae discovered to date, extending over 450 kpc around the bright quasar UM287 at  $z = 2.283$ . Characterized by high surface brightnesses over intergalactic scales, its Ly $\alpha$  emission may either trace high-density ionized gas ('clumps') or large column densities of neutral material. To distinguish between these two possibilities, information from a non-resonant line such as H $\alpha$  is crucial. Therefore, we analysed a deep Multi-Object Spectrometer For Infra-Red Exploration (MOSFIRE) observation of one of the brightest Ly $\alpha$ -emitting regions in the Slug Nebula with the goal of detecting associated H $\alpha$  emission. We also obtained a deep, moderate resolution Ly $\alpha$  spectrum of the nearby brightest region of the Slug. We detected an H $\alpha$  flux of  $F_{\text{H}\alpha} = 2.62 \pm 0.47 \times 10^{-17} \text{ erg cm}^{-2} \text{ s}^{-1}$  ( $\text{SB}_{\text{H}\alpha} = 2.70 \pm 0.48 \times 10^{-18} \text{ erg cm}^{-2} \text{ s}^{-1} \text{ arcsec}^{-2}$  at the expected spatial and spectral location. Combining the H $\alpha$  detection with its corresponding Ly $\alpha$  flux (determined from the narrow-band imaging), we calculate a flux ratio of  $F_{\text{Ly}\alpha}/F_{\text{H}\alpha} = 5.5 \pm 1.1$ . The presence of a skyline at the location of the H $\alpha$  emission decreases the signal-to-noise ratio of the detection and our ability to put stringent constraints on the H $\alpha$  kinematics. Our measurements argue for the origin of the Ly $\alpha$  emission being recombination radiation, suggesting the presence of high-density ionized gas. Finally, our high-resolution spectroscopic study of the Ly $\alpha$  emission does not show evidence of a rotating disc pattern and suggest a more complex origin for at least some parts of the Slug Nebula.

**Key words:** galaxies: haloes – galaxies: high-redshift – intergalactic medium – quasars: emission lines – cosmology: observations.

## 1 INTRODUCTION

In the standard paradigm of galaxy formation and evolution, galaxies are thought to be fuelled by accreting material from their surrounding circumgalactic medium (CGM). However, the properties of this accreting material, such as the density, temperature, angular momentum, and morphology, remain uncertain. Some cosmological simulations suggest that most of this material accretes in the form of relatively cold ( $T \sim 10^4$  K) intergalactic filaments. This has even been found to be the case for the most massive galaxies at high redshift, for which a stable hot corona should be in place (Dekel et al. 2009). On the other hand, theoretical arguments and higher resolution simulations have highlighted that such streams may not be able to survive instabilities (Nelson et al. 2013; Mandelker et al. 2016). Alternatively, such material could result from the cooling of the hot corona (Voit et al. 2015). In order to distinguish between

these two scenarios, direct imaging of the CGM and intergalactic gas is essential.

Unfortunately, the expected emission of both the cold component (due to the recombination radiation of gas ionized by the cosmic ultraviolet background) and hot component (due to X-ray bremsstrahlung) of the CGM around a typical galaxy at  $z > 2$  is well below current detection limits (e.g. Cantalupo et al. 2005; Gallego et al. 2018). Local ultraviolet (UV) radiation fields, such as in the vicinity of a bright active galactic nucleus (AGN), may be used to increase the detectability of Ly $\alpha$  emission. Indeed, in recent years, several enormous Ly $\alpha$  nebulae (ELANe) have been discovered at  $z > 2$  around bright radio-quiet quasars. ELANe are characterized by their extended Ly $\alpha$  emission that traces the CGM, and even intergalactic medium (IGM), out to several hundred kiloparsecs (kpc) from their quasars. These detections were made using custom-made narrow-band (NB) filters on the W.M. Keck I telescope (Cantalupo et al. 2014; Hennawi et al. 2015; Cai et al. 2017; Cai et al. 2018) or by performing integral field spectroscopy using the Keck Cosmic Web Imager (KCWI) (Cai et al. 2018) or the Multi Unit Spectroscopic Explorer (MUSE) on the Very Large Telescope of the European

\* E-mail: cleibler@ucsc.edu (CNL); cantalupo@phys.ethz.ch (SC)

Southern Observatory (Borisova et al. 2016; Arrigoni Battaia et al. 2018; see Cantalupo 2017 for a review).

The largest and brightest of such  $\text{Ly}\alpha$  emitting structures, nicknamed the ‘Slug Nebula’, was discovered by Cantalupo et al. (2014). The ‘Slug’ was found near the radio-quiet quasar UM287 using a custom NB filter on the Low Resolution Imaging Spectrometer (LRIS) instrument mounted on the Keck I telescope. With a total projected size of at least 480 physical kpc, this nebula extends well beyond the virial radius of the halo of a typical bright quasar host with a mass of  $\sim 10^{12.5} M_{\odot}$  (see da Ángela et al. 2008; Trainor & Steidel 2012). The UM287 Nebula (also referred to as the Slug Nebula, Slug, or Nebula throughout this paper), therefore, represents the best system available to date in which to jointly study the circumgalactic and intergalactic medium in emission.

The filamentary and asymmetric morphology of the Slug Nebula is similar to the predictions of recent cosmological simulations. However, the very high surface brightness (SB) of the  $\text{Ly}\alpha$  emission (above  $10^{-17} \text{erg s}^{-1} \text{cm}^{-2} \text{arcsec}^{-2}$ ) extending over hundreds of kpc presents a serious challenge to our current theoretical understanding of baryonic structure formation in the massive haloes associated with quasars. As discussed in Cantalupo et al. (2014), there are at least two possible scenarios for the origin of the extended  $\text{Ly}\alpha$  emission: (i) fluorescent  $\text{Ly}\alpha$  emission following hydrogen recombinations of the gas ionized by the quasar, and (ii)  $\text{Ly}\alpha$  ‘photon-pumping’ or ‘scattering’ of the quasar broad-line region emission.

In the first case, the observed  $\text{Ly}\alpha$  SB can only be explained if the recombining gas is ‘cold’ ( $T < 10^5$  K) and has very large densities ( $> 1\text{--}10 \text{cm}^{-3}$ ) that are much higher than the typical gas densities expected at such large distances from a galaxy. However, because recombination emission scales with the density squared, a small volume filling factor or a large gas clumping factor ( $C > 1000$ ) below the scale of a few kpc could explain the  $\text{Ly}\alpha$  emission as well as the much lower volume-averaged densities. Therefore, this interpretation of the data would require dense photoionized ‘clumps’ of gas within the CGM but these clumps must have sizes that are well below the current resolution limits of cosmological simulations (see e.g. Cantalupo et al. 2014, Arrigoni Battaia et al. 2015b for further discussion).

The second case, as discussed in Cantalupo et al. (2014), would require very large column densities of neutral gas above  $10^{20} \text{cm}^{-2}$  (i.e. corresponding to damped  $\text{Ly}\alpha$  systems, abbreviated as DLAs) to be present on scales of hundreds of kpc around the quasar. This material would then have to be illuminated by the  $\text{Ly}\alpha$  emission of the quasar’s broad-line region without being photoionized by the quasar itself. Although optically thick gas is routinely observed in the proximity of quasars (Prochaska et al. 2013), such large column densities of neutral material over these distance scales are not typically observed either in absorption studies or in cosmological simulations. However, recent deep observations have found that some DLAs are also associated with  $\text{Ly}\alpha$  nebulae, although these nebulae have much smaller physical scales and luminosities than the Slug (Fumagalli et al. 2017).

Either scenario therefore requires very high densities and  $\text{Ly}\alpha$  observations alone are not able to distinguish whether the gas is mostly neutral and diffuse or ionized and clumpy. In order to break this degeneracy, a non-resonant line such as  $\text{He II}[1640]$  or  $\text{H}\alpha$  is needed. In particular, a detection or limit on  $\text{H}\alpha$  emission would put the most stringent constraint on the recombination versus scattering origin of the  $\text{Ly}\alpha$  emission because these two transitions arise in the same atom. Another advantage of searching for  $\text{H}\alpha$  emission is that the presence of  $\text{He II}[1640]$  emission could require favourable

conditions in terms of the ionization spectrum and ionization parameter (see e.g. Arrigoni Battaia et al. 2015b; Cantalupo et al., in preparation).

To our knowledge, there have been no reported detections prior to our study of  $\text{H}\alpha$  emission from intergalactic gas associated with  $\text{Ly}\alpha$  nebulae around radio-quiet quasars.<sup>1</sup> Similarly, no  $\text{He II}[1640]$  emission has been found in long-slit spectroscopic observations of ELANe around radio-quiet quasars (Arrigoni Battaia et al. 2015b), although deep integral-field spectroscopic observations are now revealing  $\text{He II}$  emission at fainter levels than expected (Cantalupo et al., in preparation). In contrast with ELANe, a few detections of  $\text{He II}[1640]$  in radio-quiet  $\text{Ly}\alpha$  blobs (LABs, see Cantalupo 2017 for a review) have been reported (e.g. Prescott, Martin & Dey 2015a), though the majority of LABs show no sign of  $\text{He II}[1640]$  emission (Arrigoni Battaia et al. 2015a).

Although the terms LAB and ELAN are often used interchangeably, it is important to note some distinctions. ELANe are bright ( $L_{\text{Ly}\alpha} \sim 10^{44} \text{erg s}^{-1}$ )  $\text{Ly}\alpha$  nebulae around  $z > 2$  quasars with extents  $> 100$  kpc (e.g. Cantalupo et al. 2014; Hennawi et al. 2015; Arrigoni Battaia et al. 2018). Though comparable in size and brightness to ELANe, LABs were historically distinguished by their apparent lack of association with an AGN or bright continuum source at the time of their discovery (e.g. Steidel et al. 2000; Matsuda et al. 2004; Dey et al. 2005; Prescott, Dey & Jannuzi 2009; Yang et al. 2009; Arrigoni Battaia et al. 2015a). However, follow-up observations of LABs often uncovered evidence of the presence of obscured AGN or massively star-forming galaxies (e.g. Chapman et al. 2001; Geach et al. 2009; Overzier et al. 2013; Prescott et al. 2015b; Hine et al. 2016). Therefore, the term LABs has started being used by some authors to refer to large  $\text{Ly}\alpha$  nebulae with physical extents greater than  $\sim 100$  kpc.

Given this broader definition of LABs, ELANe could be considered a subtype of LABs. However, since LABs encompass a wide variety of systems, it would be a mistake to blindly apply any inferences about ELAN emission mechanisms to LABs as a whole. Similarly, though very extended  $\text{Ly}\alpha$  nebulae have been found around high-redshift radio-loud galaxies with large radio jets, these more commonly exhibit extended  $\text{He II}[1640]$  emission and broader kinematics. This could suggest that different processes are at play between radio-quiet and radio-loud systems (see e.g. Villar-Martín 2007, Miley & De Breuck 2008, and Cantalupo 2017 for reviews).

Nevertheless, despite the different classifications and nomenclatures associated with highly-extended  $\text{Ly}\alpha$  emission discovered in the last decades, they are almost always associated with AGN or massively star-forming galaxies. This suggests that the presence of a strong ionizing field, and therefore emission produced by fluorescent recombination radiation, is likely a necessary requirement in all cases (see Cantalupo 2017 for discussion).

In this paper, we report the results of our search for extended  $\text{H}\alpha$  emission from the Slug Nebula using long-slit near infrared (NIR) spectroscopy with the new MOSFIRE instrument on the W.M. Keck I telescope. We also perform high-resolution  $\text{Ly}\alpha$  spectroscopy of a similar region in the Slug Nebula with the goal of both guiding our  $\text{H}\alpha$  search in the velocity dimension and gaining a deeper understanding of the  $\text{Ly}\alpha$  kinematics.

The paper is organized as follows: In Section 2.1, we describe the deep Keck I/LRIS observations taken of the brightest region

<sup>1</sup>Detection of  $\text{H}\alpha$  emission from galaxies embedded in some  $\text{Ly}\alpha$  nebulae at  $z \sim 2.3$  have been reported by, for example, Yang et al. (2014)

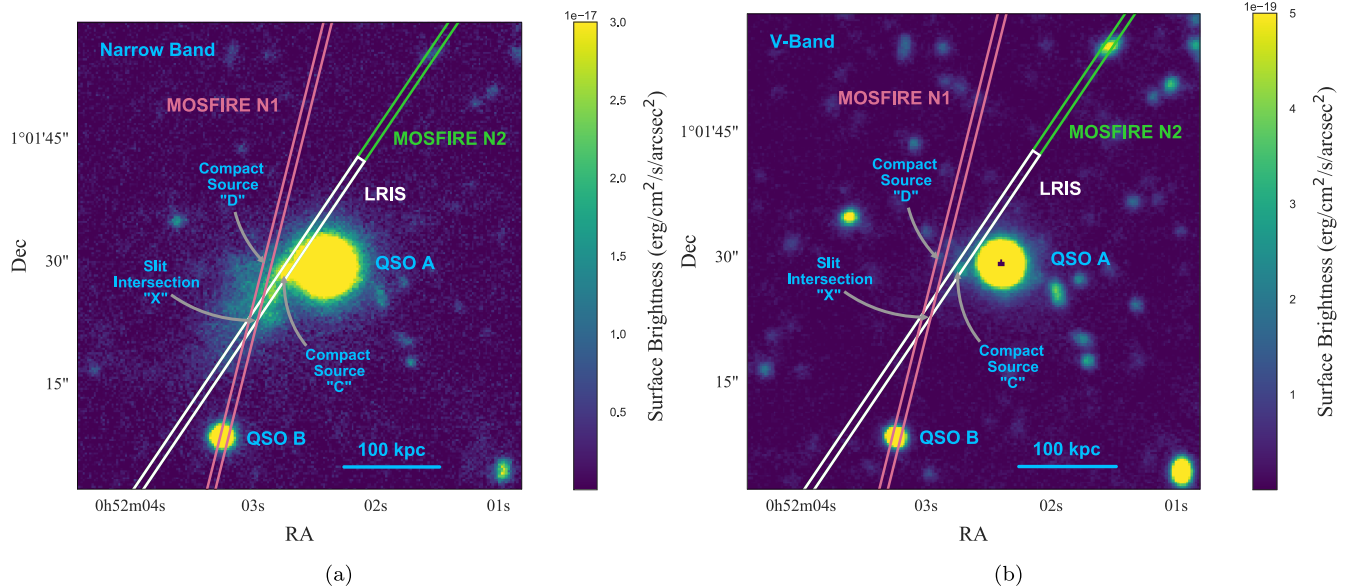


**Figure 1.** This figure depicts the 10 h NB image (left panel) and deep continuum image (right panel) of the region surrounding the UM287 Nebula, adapted from fig. 1 of Cantalupo et al. (2014). The NB data were taken on the Keck I telescope with the LRIS NB3985 filter, selected to cover Ly $\alpha$  emission at the redshift of QSO A. The continuum image was taken simultaneously with the LRIS V-band filter on the red camera. The MOSFIRE Night 1 (N1), MOSFIRE Night 2 (N2), and LRIS slit positions are overlaid in red, green, and white, respectively. The green MOSFIRE N2 slit extends the full length of the image, overlapping with the white LRIS slit. QSO A, QSO B, compact source ‘C’, compact source ‘D’, and position ‘X’ (the intersection of the MOSFIRE N1 and LRIS slits), are also labelled.

of the Slug Nebula and in Section 2.2, discuss the data reduction process of these observations. Similarly, the two nights of deep NIR spectroscopy, obtained using Keck I/MOSFIRE, and their reduction, are described in Sections 2.3 and 2.4, respectively. In Section 3.1, we explore the Ly $\alpha$  kinematics of the Slug and in Section 3.2 we measure the Ly $\alpha$  flux contained within the MOSFIRE N1 slit. Sections 3.3 and 3.4.1 discuss the measurement of the Slug Nebula’s H $\alpha$  flux. We also extract the 1D spectra of two compact sources in the vicinity of the Slug Nebula ( $z \sim 2.287$ ) from the MOSFIRE Night 1 and Night 2 observations in Section 3.5, and calculate their N II and H $\alpha$  fluxes. In Section 4.1, we examine the implications of the Ly $\alpha$  kinematics for the Nebula’s gas distribution. In Section 4.2, we compute the Ly $\alpha$  to H $\alpha$  flux ratio and compare it to predictions from case B recombination radiation. In Section 4.3, we constrain the emission origin for compact sources ‘C’ and ‘D’ (AGN versus star-formation versus QSO A fluorescence). Finally, in Section 5, we summarize our results.

## 2 OBSERVATIONS

### 2.1 LRIS spectroscopy

On UT 2015 September 09, we used the blue camera of the Low-Resolution Imaging Spectrometer (LRIS; Oke et al. 1995) on the Keck I 10 m telescope to observe the Ly $\alpha$  emission of the UM287 Nebula. The spectra were obtained with a 1 arcsec slit as part of a multi-object slit mask. The slit was oriented with a position angle (PA) of  $322^\circ$ , to match the PA of the MOSFIRE Night 2 (N2) mask (see Fig. 1). In order to cover the Ly $\alpha$  emission of the Slug, we used the D460 dichroic and the 1200 lines  $\text{mm}^{-1}$  grism blazed at  $3400 \text{ \AA}$ , which covers  $\approx 3300\text{--}4200 \text{ \AA}$ . The measured full-width at half-max (FWHM) was found to be  $\sim 1$  arcsec. We acquired  $9 \times 1800 \text{ s}$  science exposures, for a total exposure time of 4.5 h. In between each exposure, we dithered  $\sim 1$  arcsec along the slit.

In addition to the science exposures, we took bias frames, arcs, as well as slitless and slitted twilight flats, which were used in the data reduction process. All exposures were read out with  $1 \times 1$  CCD binning.

### 2.2 LRIS calibrations and data reduction

The LRIS blue camera data were reduced using the publicly available LOWREDUX package, distributed within XIDL (Prochaska, Hennawi & Burlles 2017) producing nine calibrated, unfluxed 2D spectra. This pipeline performs standard data reduction steps, including overscan and bias subtraction, flat fielding, and wavelength calibration.

The flat fielding procedure constructs a pixel flat used to correct for pixel sensitivity variation from the slitless twilight flats. In addition, the slitted twilight flats are utilized to correct for the non-uniform illumination of the slit. LOWREDUX determines a wavelength solution by fitting low-order polynomials to the arc lamp spectra and is reported in air wavelengths for the 2D spectra.

We wrote custom PYTHON scripts using the ASTROPY (Astropy Collaboration 2013), IPYTHON (Perez & Granger 2007), MATPLOTLIB (Hunter 2007), NUMPY (Walt, Colbert & Varoquaux 2011), and SCIPY (Jones et al. 2001) packages, to coadd the individual reduced spectra since LOWREDUX does not combine 2D spectra. Due to the dithering along the slit between exposures, each image needed to be shifted, in the spatial direction, to a common frame (chosen to be that of the fifth exposure). To calculate the required shift, we fit Gaussians to the spatial profile of a star in a separate slit on the mask and determined the change in the centroid position. The applied shifts were rounded to the nearest integer pixel in order to avoid interpolation and complications in calculating the associated error. The uncertainty associated with integer shifts is at most 1/2 pixel, which corresponds to an error of 0.0675 arcsec, which is far less than the 1 arcsec seeing disc.

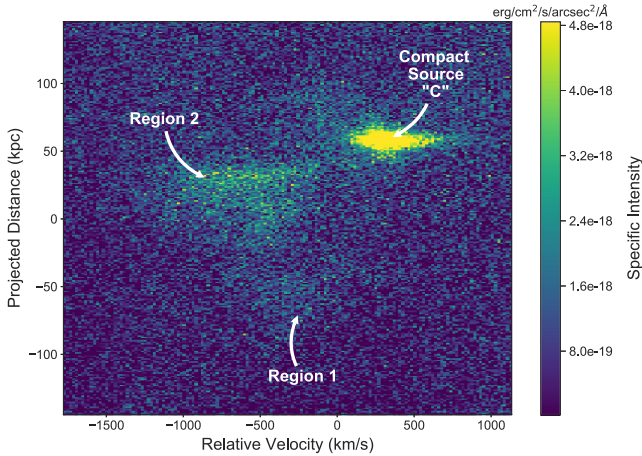


**Figure 2.** The unsmoothed 2D spectrum taken with Keck I/LRIS (the white slit in Fig. 1). The  $v = 0 \text{ km s}^{-1}$  corresponds to the expected  $\text{Ly}\alpha$  emission at a redshift of  $z = 2.283$ , the redshift of QSO A. The projected distance corresponding to 0 kpc indicates the location of the MOSFIRE N1 and LRIS slit intersection, referred to as position ‘X’ in Fig. 1. The bright  $\text{Ly}\alpha$  emitter around  $v \sim 300 \text{ km s}^{-1}$  and spatial position of  $\sim 60 \text{ kpc}$  is compact source ‘C’ (see Fig. 1). The Slug Nebula has a physical extent along the slit of  $\sim 150 \text{ kpc}$ . Its  $\text{Ly}\alpha$  emission is blue-shifted with respect to that of compact source ‘C’ ( $z = 2.287$ ) and the redshift of QSO A ( $z = 2.283$ ).

LRIS is known to experience significant telescope pointing position-dependent flexure, which shifts the location of a fixed wavelength on the detector. `LOWREDUX` uses the known wavelengths of skylines to measure, in an extracted 1D spectrum, the wavelength solution offset caused by the flexure. We therefore used `LOWREDUX` to extract a 1D spectrum of compact source ‘C’ (see Fig. 2), which is located in the same slit as the Slug Nebula, and calculated the flexure-induced spectral pixel shift for each exposure. This shift of  $\sim 11\text{--}13$  unbinned pixels was then rounded to the nearest integer pixel and applied in the spectral direction of each of the 2D spectra. The rounding error of at most  $1/2$  pixels amounts to an uncertainty of  $\approx 0.135\text{\AA}$  or  $\approx 10 \text{ km s}^{-1}$ .

Once the exposures were corrected for flexure and dithering offsets, we ran each of them through the publicly distributed `DCR` package (Pych 2004, 2012) to detect and remove cosmic rays. We then coadded these nine cleaned images by summing the electron counts in each pixel and renormalizing by the total exposure time. In addition, the corresponding 2D wavelength fits file produced by `LOWREDUX` was converted from air wavelengths to vacuum wavelengths.

Lastly, we flux calibrated our coadded spectrum using the deep NB imaging of the UM287 field presented in Cantalupo et al. (2014). In order to do so, we applied the LRIS slit to the NB image, choosing only the pixels that contributed to the flux in our spectrum. Next, we trimmed off the outer edges of the slit, selecting the region of the spectrum that has flux from the Nebula and very good background subtraction. We then summed up the NB flux within this shortened slit, which was four binned pixels wide by 135 binned pixels long and covered  $1.08 \text{ arcsec}$  by  $36.45 \text{ arcsec}$  on the sky.

This total NB flux is compared to that of the 2D spectrum over the same wavelength range and spatial location. The equivalent flux of the 2D spectrum is calculated by first applying the filter transmission function to the spectral direction of the spectrum. We then integrate the flux, in  $\text{e}^{-}\text{s}^{-1}$ , over the shortened slit region and divide the total NB flux by the summed 2D spectrum flux to compute the conversion factor from  $\text{e}^{-}\text{s}^{-1}$  to  $\text{erg cm}^{-2} \text{ s}^{-1}$ . This conversion

**Table 1.** Coordinates for the MOSFIRE Mask Targets. We also include here the coordinates of QSO A for completeness.

Target name	RA (J2000)	Dec (J2000)	Slitlet #
2MASS Star 1	00 <sup>h</sup> 51 <sup>m</sup> 54 <sup>s</sup> .26	+01 <sup>o</sup> 03 <sup>′</sup> 21 <sup>″</sup> .2	1
QSO A	00 <sup>h</sup> 52 <sup>m</sup> 02 <sup>s</sup> .40	+01 <sup>o</sup> 01 <sup>′</sup> 29 <sup>″</sup> .3	N/A
UM287 Nebula	00 <sup>h</sup> 52 <sup>m</sup> 02 <sup>s</sup> .99	+01 <sup>o</sup> 01 <sup>′</sup> 23 <sup>″</sup> .1	2
QSO B (Night 1 only)	00 <sup>h</sup> 52 <sup>m</sup> 03 <sup>s</sup> .26	+01 <sup>o</sup> 01 <sup>′</sup> 08 <sup>″</sup> .6	2
2MASS Star 2	00 <sup>h</sup> 52 <sup>m</sup> 07 <sup>s</sup> .78	+00 <sup>o</sup> 59 <sup>′</sup> 06 <sup>″</sup> .9	3

factor is then applied to each pixel of the LRIS spectrum to produce a fully flux-calibrated 2D spectrum.

In order to use an integer number of pixels, the width of the NB-shortened slit corresponds to  $1.08 \text{ arcsec}$  which is slightly bigger than the LRIS slit width of  $1 \text{ arcsec}$ . Therefore, we expect the flux-calibration of the LRIS spectrum to be biased slightly high, by approximately 8 per cent. To estimate the systematic error on our flux calibration, we calculated the flux of the compact source, marked as ‘C’ in Figs 1 and 2. We find that the compact source flux in the NB and spectrum differ by 20 per cent, which we will take to be our systematic uncertainty.

### 2.3 MOSFIRE spectroscopy

We observed the Slug Nebula on 2014 October 02 (Night 1 or N1) and 2014 October 03 (Night 2 or N2), using the MOSFIRE instrument (McLean et al. 2010, 2012) on the Keck I 10 m telescope. The spectra were taken using the *K*-band grating so as to cover the expected  $H\alpha$  emission ( $\lambda 6562.8$ ) of the Nebula ( $z \sim 2.283$ ), with a total wavelength coverage of  $19540\text{--}24060 \text{\AA}$ . We used a  $1 \text{ arcsec}$  slit width for both nights of observation, resulting in a spectral resolution of  $R \sim 2500$  at  $\lambda = 21545.67 \text{\AA}$ .

The two masks we designed had three slitlets; the middle slitlet was centred on a region of the UM287 Nebula predicted to have the highest  $H\alpha$  emission, while the top and bottom slitlets were aligned on two stars from the Two Micron All Sky Survey (2MASS). All coordinates are shown in Table 1. These 2MASS stars were included to help locate the exact position of the UM287 Nebula in case of a non-detection as well as to help track the drift of the mask across the detector (see Kriek et al. 2015).

For the first night, we used a slit at a PA of  $342^\circ$ . We observed using an AB’BA’ dither pattern with offsets of  $+51, -17, +17, -51 \text{ arcsec}$ , respectively, and exposure times of  $119.3 \text{ s}$  for a total integration of  $4.8 \text{ h}$ . The median seeing during Night 1 was about  $0.7 \text{ arcsec}$  for both nights but there were intermittent cirrus clouds such that the conditions were not photometric. So as to cover a larger area of the Nebula, we used a different PA for Night 2 of  $322^\circ$ , centred on the same patch of Nebula as for Night 1 (see Fig. 1). We observed using the same AB’BA’ dither pattern and exposure times as for Night 1, for a total integration of  $2.6 \text{ h}$ . Both slit orientations are shown in Fig. 1.

### 2.4 MOSFIRE calibrations and data reduction

At the beginning of each night, we took neon and argon arcs through the masks as well as dome flats and thermal flats. Immediately prior to observing UM287, we took spectroscopic standards of HIP5164 with a  $1 \text{ arcsec}$  longslit on Night 1 and a  $0.7 \text{ arcsec}$  longslit on Night 2. These were used to flux calibrate our data as well as correct for telluric absorption. Since we only observed HIP5164 once in

the evening, we cannot account for any changes to the telluric absorption throughout the night.

The UM287 data, as well as the standard HIP5164, were reduced using the publicly available MOSFIRE Data Reduction Pipeline (version 2016 August; DRP; Steidel et al. 2014). The DRP first flat fields the images and traces the slit edges. To correct for the dome's emission of  $K$ -band wavelength photons, the software subtracts the thermal flats from the dome flats before creating a normalized combined flat. Next, the code combines exposures and preforms the wavelength calibration, combining an interactive fitting of the night skylines with neon and argon arcs to correct for the faintness of the skylines at the reddest wavelengths. The sky background is then subtracted and the images are rectified, producing a 2D spectrum for each slitlet along with their corresponding noise frames and integration time maps.

To prevent smearing out the emission due to the mask drift across the detector over the course of our observations (see for instance, Kriek et al. 2015), we reduced our Night 1 data in six batches of 24 exposures ( $\sim 48$  min) each (other than the last batch which only had 23 exposures). We then measured the mask drift between batches by tracking the centroids of the two 2MASS stars (see Table 1) also present in the MOSFIRE mask. We found shifts of  $\pm 1$ –2 pixels (0.18–0.36 arcsec) between batches which we corrected for before coadding the data. Due to the shortness of the Night 2 observations and the shifts of only about 1 pixel found in the Night 1 data over the course of  $\approx 1$  h, we did not bother correcting for mask drift in the Night 2 data.

In order to flux calibrate our UM287 Nebula 2D spectrum, we used the spectrum of the A0 standard star HIP5164. The 1D spectrum of HIP5164 was derived from the 2D spectrum returned by the DRP, using a boxcar extraction that assumes a Gaussian spatial profile. We then calculated the sensitivity function by comparing this 1D spectrum to a template spectrum of Vega from Bohlin (2014) that has the NIR emission from the debris disc removed. That spectrum was then renormalized to have the same 2MASS magnitude as HIP5164. This sensitivity function, as well as a simple slit loss correction to account for the finite slit width, was applied to achieve the final flux calibrated UM287 Nebula 2D spectrum, shown in Fig. 2.

### 3 ANALYSIS AND RESULTS

The final 2D LRIS and MOSFIRE spectra are shown in Figs 2 and 3. In this section, we first examine the kinematics of the Slug Nebula. In Section 3.1, we calculate the first and second moments of the LRIS  $\text{Ly}\alpha$  spectrum to determine the kinematic structure and gas distribution of the Nebula. Next, we measure the  $\text{Ly}\alpha$  (Section 3.2) and  $\text{H}\alpha$  (Section 3.3) flux emitted by the brightest part of the Slug, using the LRIS NB image and MOSFIRE N1 spectrum, respectively. In Section 3.4.1 we derive the  $\text{Ly}\alpha$  to  $\text{H}\alpha$  ratio, which will help us constrain the mechanism powering the Slug Nebula's  $\text{Ly}\alpha$  emission. Finally, we compute the  $\text{H}\alpha$  and corresponding  $\text{N II}[6583]$  line fluxes of compact sources 'C' and 'D' in Section 3.5.

#### 3.1 The $\text{Ly}\alpha$ kinematics

The velocity centroid and velocity dispersion as a function of spatial position for the  $\text{Ly}\alpha$  emission around the Slug Nebula is shown in the top left and top right panels of Fig. 4, respectively. To calculate these kinematic tracers, we first selected an appropriate region

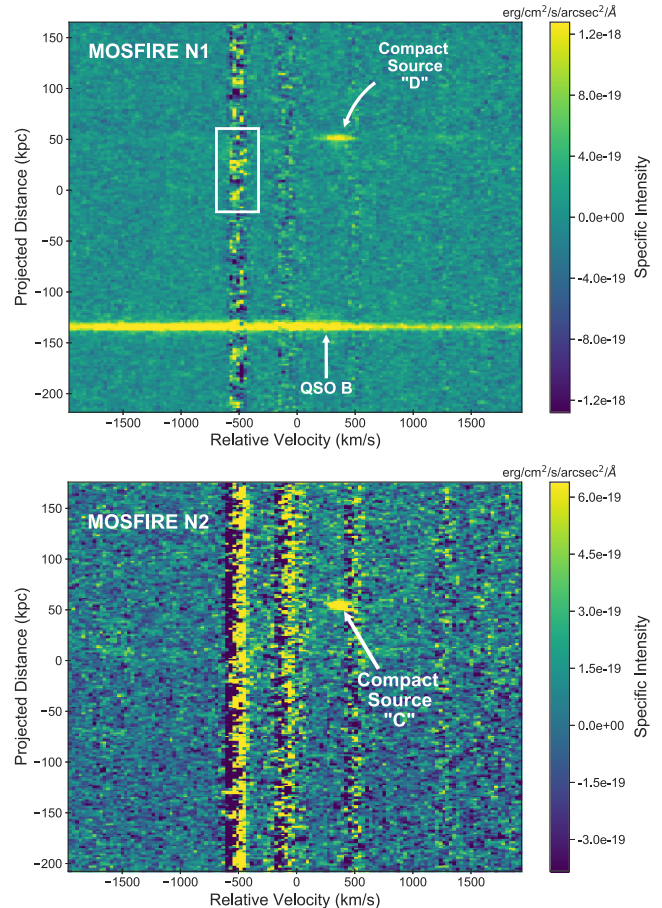


**Figure 3.** The top panel shows the unsmoothed 2D spectrum taken with Keck I/MOSFIRE (4.8 h) using the N1 slit orientation (the red slit in Fig. 1). The  $v = 0$  km s $^{-1}$  corresponds to the expected  $\text{H}\alpha$  emission at a redshift of  $z = 2.283$ , the redshift of QSO A. The spatial offset of 0 kpc indicates the location of the MOSFIRE N1 and LRIS slit intersection, referred to as position 'X' in Fig. 1. The white rectangle indicates the region in which the  $\text{H}\alpha$  flux of the Slug was measured (see Section 3.3.1 for a description of how the dimensions and location of the rectangle were chosen). Note that the flux measurement aperture overlaps with the continuum emission from compact source 'D'. This contaminant is masked out when we perform any analyses or measure fluxes. The bright continuum source around  $\sim 150$  kpc is QSO B. The  $\text{H}\alpha$  and  $\text{N II}[6583]$  emission lines of compact source 'D' ( $z = 2.287$ ) are visible at a spatial position of  $\sim 50$  kpc and spectral positions of  $\sim 400$  km s $^{-1}$  and  $\sim 1200$  km s $^{-1}$ , respectively. The bottom panel shows the unsmoothed 2D spectrum taken with Keck I/MOSFIRE (2.6 h) using the N2 slit orientation (the green slit in Fig. 1). The spectral and spatial axes match those of the N1 spectrum and their zero-points are defined in the same way as in the top panel. The emission line at  $\sim 400$  km s $^{-1}$  and  $\sim 50$  kpc is the  $\text{H}\alpha$  line of compact source 'C' ( $z = 2.287$ ).

around the Slug Nebula. We started by running CUBEXTRACTOR (Cantalupo, in preparation; see also Borisova et al. 2016 and Marino et al. 2018 for a short description) on the LRIS 2D spectrum with spatial and wavelength Gaussian smoothing of  $\sigma = 2$  pixels and a signal-to-noise threshold of 3 per smoothed pixel. The resulting region is shown in the bottom left panel of Fig. 4.

Next, we partitioned the spatial extent of  $\text{Ly}\alpha$  emission into bins of five pixels (5.68 kpc). Note that these are not independent regions since the seeing in the spatial direction was  $\sim 10$  pixels but this box size allows us to finely sample the kinematics of the transition region between the Slug Nebula and compact source 'C'. We then

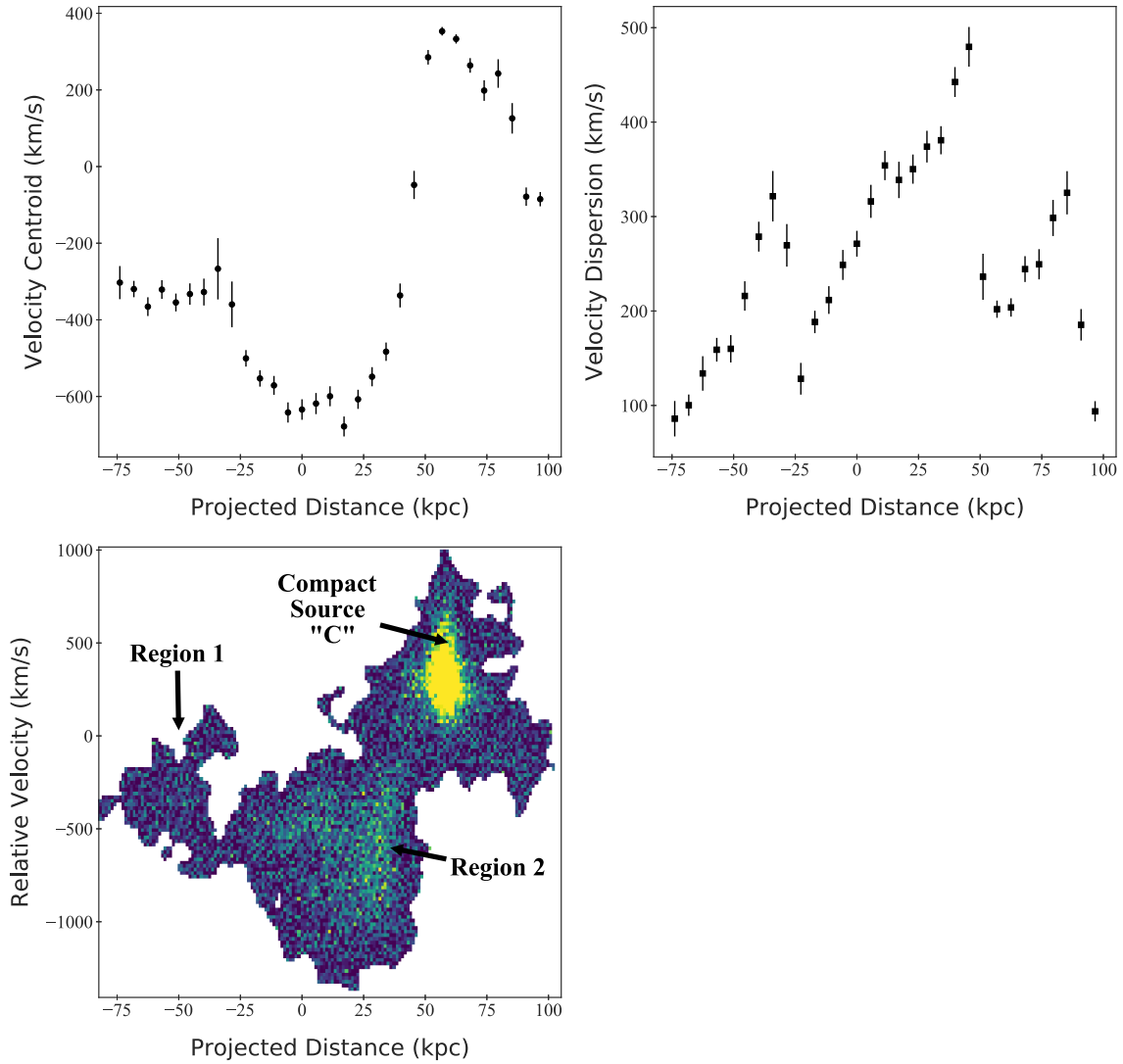


**Figure 4.** The  $\text{Ly}\alpha$  kinematics of the region around the Slug Nebula. The flux-weighted first moment of the velocity distribution, also referred to as the velocity centroid, is plotted as a function of position along the slit in the top left panel. The velocity centroid was calculated according to equation (1), within spatial bins of five pixels. Similarly, the flux-weighted second moment of the velocity distribution about the flux-weighted mean, which we refer to as the velocity dispersion, was calculated according to equation (2). The velocity dispersion in spatial bins of five pixels is shown as a function of projected distance along the slit in the top right panel of this figure. In both top panels, the  $1\sigma$  error bars were computed using standard bootstrapping techniques. The area of  $\text{Ly}\alpha$  emission used to measure the velocity centroid and dispersion only includes pixels with a  $\text{SNR} \geq 3$ , and is depicted in the bottom left panel (the colour bar matches that of Fig. 2). The  $v = 0 \text{ km s}^{-1}$  corresponds to the expected  $\text{Ly}\alpha$  emission at the redshift of QSO A ( $z = 2.283$ ). The projected distance of 0 kpc indicates the location of the MOSFIRE N1 and LRIS slit intersection. Three distinct spatial regions, with different kinematic properties, are apparent in both the velocity centroid and velocity dispersion plots: the dimmer left-most region of the Nebula (Region 1), the brighter region of the Nebula to the right (Region 2) and the compact source ‘C’ area in the right-most part of the figure.

calculated the flux-weighted first and second moments of the  $\text{Ly}\alpha$  velocity distribution for each spatial bin according to equations (1) and (2).

$$V_{\text{cent}} = \frac{\sum v F(v)}{\sum F(v)}, \quad (1)$$

$$V_{\text{disp}} = \sqrt{\frac{\sum (v - V_{\text{cent}})^2 F(v)}{\sum F(v)}}. \quad (2)$$

The flux-weighted mean velocity, which we also refer to as the centroid velocity, is presented in the left panel of Fig. 4 as a func-

tion of spatial distance from point ‘X’ (the intersection point of the Night 1 and Night 2 slits denoted in Fig. 1). The standard error on the velocity centroid, for each spatial bin, was determined using statistical bootstrapping and is shown as the black error bars. Since each spatial bin is about half the size of the atmospheric seeing, each of these bins are correlated. Therefore, the bootstrapped errors are likely an underestimate of the true errors.

As seen in the top left panel of Fig. 4, the kinematics indicate that the Slug Nebula, the part of the spectrum between 35 kpc and  $-75$  kpc, is comprised of two regions with distinct kinematics. The first one, which we call ‘Region 1’, is located at  $\sim -50$  kpc and

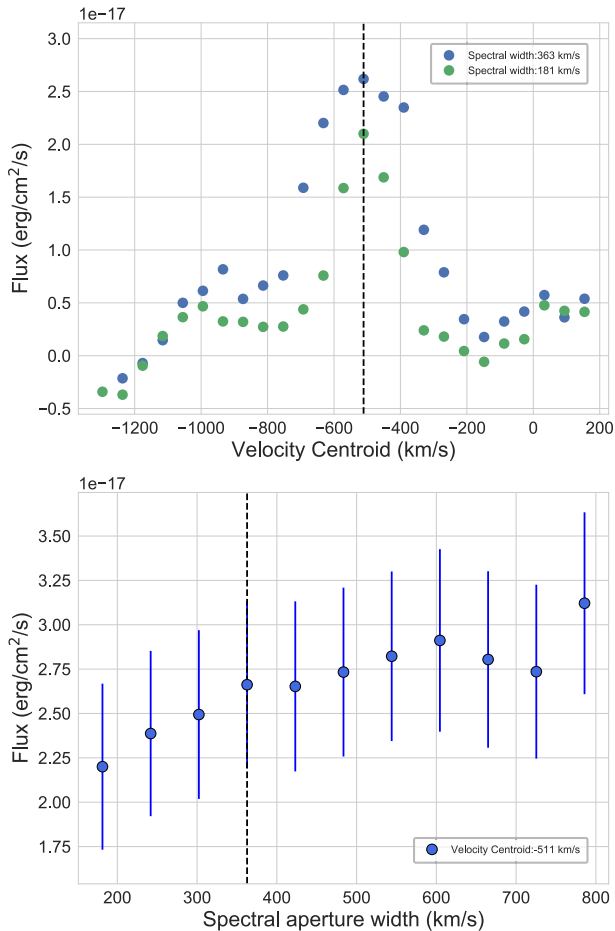


**Figure 5.** Though the spatial aperture size and centroid can be determined empirically from the NB Ly  $\alpha$  image (see Fig. 1), radiative transfer effects can modify the kinematics of the Ly  $\alpha$  such that it cannot be used to inform the expected wavelength of the H  $\alpha$  emission. To determine the most likely velocity centroid, we calculated the flux as a function of velocity position within a narrow velocity window (six pixels/181 km s<sup>-1</sup>), as shown in green in the top panel of this figure. The velocity that maximized the flux, -511 km s<sup>-1</sup>, was chosen as the centroid position. Note that doubling the velocity window does not change the location of the peak (shown in blue). We used a flux curve-of-growth approach to determine the optimal spectral window size. The flux within the MOSFIRE aperture (centred at the velocity centroid of -511 km s<sup>-1</sup>) is shown in the bottom panel as a function of velocity-aperture width. At a spectral width of 363 km s<sup>-1</sup>, the H  $\alpha$  flux starts to level off. We therefore choose this as the size of the velocity width of our aperture when calculating the Slug’s H  $\alpha$  flux. The flux within these aperture dimensions result in a SNR of  $\sim 5.6\sigma$ .

has a velocity centroid of  $-333 \pm 12$  km s<sup>-1</sup>, while the second, referred to as ‘Region 2’, is at  $\sim 25$  kpc and is centred at  $-555 \pm 8$  km s<sup>-1</sup>. There is then a sharp transition around  $\sim 40$  kpc marking the beginning of compact source ‘C’, which is centred at a velocity of  $254 \pm 8$  km s<sup>-1</sup>.

The top right panel of Fig. 4 shows the flux-weighted velocity dispersion of the Ly  $\alpha$  emission as a function of the projected distance from point ‘X’. The corresponding error bars for the velocity dispersion were also computed using statistical bootstrapping. As with the velocity centroid, the velocity dispersion of the Slug Nebula displays the same demarcations between the two regions that comprise the Slug and compact source ‘C’. Their representative

velocity dispersions are  $217 \pm 7$ ,  $418 \pm 6$ , and  $453 \pm 9$  km s<sup>-1</sup>, respectively.

### 3.2 The Ly $\alpha$ flux of the Slug Nebula

We used the NB image (see the top panel of Fig. 1) to calculate the Ly  $\alpha$  flux of the Slug Nebula in the region defined within the MOSFIRE Night 1 slit, coincident with where we measure the H  $\alpha$  emission in Section 3.4.1. So that comparisons to the MOSFIRE data would be as accurate as possible, we chose the same spatial width and centroid as was used to compute the H  $\alpha$  flux (see Section 3.4.1). Though we could not precisely select the same velocity range, comparing the NB and continuum images shows that there are no continuum sources that could be contaminating the Ly  $\alpha$  measurement in our region of interest. In addition, the NB filter covers a much larger spectral window than the velocity dispersion of the Nebula (see Fig. 4), ensuring that all of the Ly  $\alpha$  velocities included in the spectrum are also included in the NB flux measurement.

Integrating over the region defined by the overplotted MOSFIRE N1 slit within the aforementioned spatial window spanning  $\sim 81.76$  kpc, results in a total Ly  $\alpha$  flux of  $F_{\text{Ly}\alpha} = 1.44 \pm 0.10 \times 10^{-16}$  erg cm<sup>-2</sup> s<sup>-1</sup> (equivalent to a surface brightness of  $\text{SB}_{\text{Ly}\alpha} = 1.48 \pm 0.10 \times 10^{-17}$  erg cm<sup>-2</sup> s<sup>-1</sup> arcsec<sup>-2</sup>).

### 3.3 The H $\alpha$ emission of the Slug Nebula

#### 3.3.1 Determining the optimal aperture for H $\alpha$ detection and flux measurement

The large spatial scale (and possibly, the large velocity width) of the H  $\alpha$  emission expected from the Slug Nebula necessarily requires spatial and spectral binning of our original data presented in Fig. 3. Moreover, we do not know a priori where the spatial and velocity centre of such an aperture should be located.

In this section, we discuss how we obtained the optimal rectangular aperture for the detection of the Slug’s H  $\alpha$  emission. Because of the lower exposure time and higher systematic noise of the MOSFIRE Night 2 observations (see Fig. 3), we will limit our search for, and analysis of, extended emission to the MOSFIRE Night 1 observations here and in the remainder of the paper. However, we will make use of the MOSFIRE N2 observations for the spectral analysis of compact source ‘C’.

As discussed in this section, we find that the optimal aperture has a spatial dimension of  $\sim 81.76$  kpc and is centred a distance of  $\sim 19.68$  kpc from the intersection of the MOSFIRE N1 and N2 slits. The optimal spectral dimension has a width of 363 km s<sup>-1</sup> centred at a velocity of  $-511$  km s<sup>-1</sup> with respect to the systemic velocity of H  $\alpha$  at a redshift of  $z = 2.283$  (the systemic redshift of the UM287 quasar obtained from CO observations; Decarli et al, in preparation).

The spatial scale and centre were chosen based on the intersection of the MOSFIRE N1 slit with the Ly  $\alpha$  NB emission. The NB Ly  $\alpha$  surface brightness was first rescaled to an expected H  $\alpha$  surface brightness assuming a case B recombination ratio of  $\text{SB}_{\text{Ly}\alpha}/\text{SB}_{\text{H}\alpha} = 8.1$ . We then calculated a  $3\sigma$  contour, assuming an estimated MOSFIRE H  $\alpha$  surface brightness error of  $1\sigma = 3.7 \times 10^{-19}$  erg cm<sup>-2</sup> arcsec<sup>-2</sup> s<sup>-1</sup>. The region within the intersections of the Night 1 slit and the  $3\sigma$  contour was 9.71 arcsec long and centred a distance of 2.34 arcsec from the intersection of the N1 and N2 slits (point ‘X’). Assuming a redshift of  $z = 2.283$ , this translates to a spatial aperture in which to calculate the H  $\alpha$  flux of  $\sim 81.76$  kpc centred at a distance of  $\sim 19.68$  kpc from point ‘X’.

We then determined the optimal spectral aperture width and central velocity. In the absence of radiative transfer effects influencing the velocity distribution of the  $Ly\alpha$  emission, we would expect the  $H\alpha$  emission to be centred close to the velocity centroid of the  $Ly\alpha$ , found to be at  $-555 \text{ km s}^{-1}$  in Section 3.1. However, possible asymmetries in the  $Ly\alpha$  due to scattering effects could bias our determination of the precise  $H\alpha$  central velocity.

In order to allow for this possibility, we chose a ‘priorless’ approach to determining the velocity centroid and width of the  $H\alpha$  emission. Rather than select the velocity centroid based on its expected location, we took a curve-of-growth approach, finding the central velocity in a wide velocity window (shown in the top panel of Fig. 5), that maximized the  $H\alpha$  flux. We first masked out the compact source continuum emission located at  $\sim 50 \text{ kpc}$  from the slit intersection ‘X’, then the  $H\alpha$  flux was measured assuming a narrow velocity window of  $181 \text{ km s}^{-1}$  (six pixels) so as to finely sample the velocity range. The  $H\alpha$  flux peaks at a velocity centroid of  $-511 \text{ km s}^{-1}$ , a result that is corroborated if we double the velocity width to  $363 \text{ km s}^{-1}$ , as shown in the top panel of Fig. 5. The curve-of-growth determined velocity centroid of  $-511 \text{ km s}^{-1}$  is extremely close to the velocity centroid of the  $Ly\alpha$  Region 2 emission, which was measured to be  $-555 \text{ km s}^{-1}$ .

Finally, we determined the spectral aperture width, which cannot simply be obtained from the breadth of the  $Ly\alpha$  emission, since radiative effects can broaden the width of this resonant line. Instead, we varied the spectral aperture width from  $181$  to  $784 \text{ km s}^{-1}$  and selected the width at which the measured  $H\alpha$  flux leveled off. As shown in the bottom panel of Fig. 5, the optimal velocity aperture has a width of  $363 \text{ km s}^{-1}$ .

Since this curve-of-growth approach to finding the velocity centroid and width of the flux aperture seeks to maximize the  $H\alpha$  flux, one could be concerned that this approach would consistently bias our  $H\alpha$  flux towards higher values. In order to quantify this effect, we used the same methodology described above to find the peak  $H\alpha$  flux in several ‘pure-sky’ background regions. When we varied the velocity centroid and width of the flux apertures, we consistently found that the maximum  $H\alpha$  peaks exceeded the mean flux value in that sky background region by up to about  $5 \times 10^{-18} \text{ erg cm}^{-2} \text{ s}^{-1}$ . Therefore, we conclude that this ‘priorless’ aperture selection would inflate the  $H\alpha$  flux by  $\leq 5 \times 10^{-18} \text{ erg cm}^{-2} \text{ s}^{-1}$ . We emphasize that our estimate is an upper limit, as it is unlikely that a statistical fluctuation would land near or on top of the detected  $H\alpha$  flux.

### 3.3.2 An empirical estimate of the sky noise

We determined an empirical noise estimate by calculating the standard deviation of the flux in ‘pure-sky’ regions. These regions were chosen so as to avoid the expected spatial location of Slug  $H\alpha$  emission as well as the outer edges of the slit, which have a reduced total exposure time. We measured the flux in these background regions using the same-sized rectangular aperture and velocity centroid as when measuring the Slug Nebula flux (see Section 3.4.1). We found that these fluxes were dominated by a linearly varying, spatially-dependent background gradient, which we modelled and removed prior to calculating the flux scatter for the pure-sky regions. We note that the removal of this background model does not affect our measurement of the Slug’s  $H\alpha$  flux since the estimated background was very close to zero at that spatial position.

The pure-sky fluxes, with the background gradient removed, are plotted in Fig. 6 as unfilled blue squares. The  $\pm 1\sigma$  standard devi-

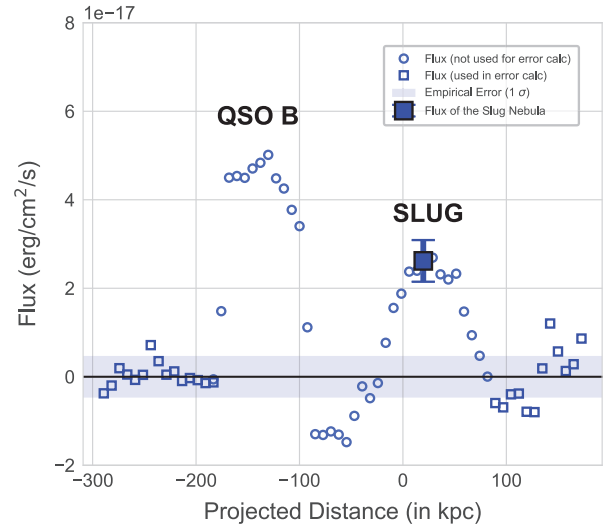


**Figure 6.** The  $H\alpha$  flux computed within rectangular apertures of size  $81.76 \text{ kpc}$  by  $363 \text{ km s}^{-1}$ , measured as a function of spatial position along the MOSFIRE N1 slit. For all these flux calculations, the apertures were centred at a velocity of  $-511 \text{ km s}^{-1}$ . The bigger dark-blue filled square marks the flux at the expected location of the Slug Nebula (see Fig. 3). The light-blue points with much higher flux values ( $\sim -75$  to  $\sim 75 \text{ kpc}$ ) are associated with the QSO B emission. The small darker-blue unfilled squares correspond to regions far enough away from the expected location of the Slug Nebula to be considered ‘pure-sky’. The error on the measurement of the Slug Nebula flux was calculated using the standard deviation of the flux in these pure-sky apertures. We note here that the pure-sky regions have a background gradient removed but the rest of data do not, see Section 3.3.2 for details. The  $\pm 1\sigma$  error is shown as the transparent blue region as well as the blue error bars associated with the Slug Nebula flux (large dark-blue square). The flux at the location of the Slug Nebula corresponds to a  $\sim 5.6\sigma$  detection.

ation of the sky fluxes (our empirical noise estimate) is shown as the transparent blue shaded region. The light-blue unfilled circles show the flux at spatial locations close to the expected  $H\alpha$  emission and were not included in the calculation of our noise estimate. The background gradient was not removed at the location of the light-blue unfilled circles. The flux at the location of the Slug is represented by the larger filled dark-blue square and corresponds to a  $\sim 5.6\sigma$  detection.

### 3.4 Examining the robustness of the Slug Nebula $H\alpha$ detection

It is important to note that our chosen velocity centroid is coincident with the skyline at  $20517 \text{ \AA}$ . The presence of a bright, imperfectly subtracted skyline at the location of our  $H\alpha$  detection might cause concern that the observed  $H\alpha$  flux within our chosen aperture is due to variance in the skyline rather than emission from the Slug Nebula.

The idea that the emission within our aperture is uncharacteristic of the variance of the skyline is corroborated by the fact that the signal to noise also peaks at the same velocity centroid as the flux. The error used in the SNR was empirically calculated by taking the standard deviation of the flux in apertures along the skyline (see Section 3.3.2). Therefore, if the emission in our aperture was typical of the skyline, this would be reflected in the noise estimate. While the flux could be biased by the presence of a skyline, the signal-to-noise ratio should be much less susceptible to this effect. The velocity centroid corresponding to the peak SNR was unchanged

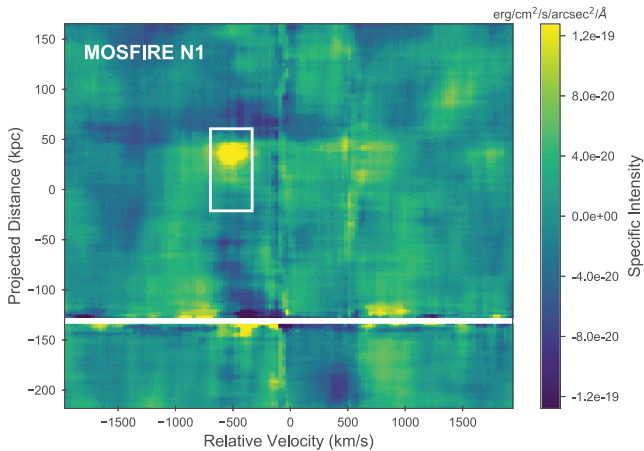


**Figure 7.** The smoothed MOSFIRE N1 2D spectrum produced using a median filter with a smoothing kernel of 41 kpc (27 pixels) in the spatial direction and  $363 \text{ km s}^{-1}$  (12 pixels) in the spectral direction. These dimensions correspond to half the size of the white rectangular aperture that was used to measure the  $\text{H}\alpha$  flux. Prior to smoothing, the continuum and line emission from compact source ‘D’ as well as QSO B were masked out. Since the median-smoothing filter does not conserve flux, this figure is meant to be purely illustrative and was not used for any of the measurements in the analysis. Though the  $\text{H}\alpha$  detection lies on top of a relatively bright skyline, we argue in Section 4.2.1 that the emission is produced by the Slug Nebula rather than high-variance pixels in the skyline residual.

whether we used our empirical noise estimate or a noise estimate calculated from the error array produced by the MOSFIRE DRP.

As an additional test of the validity of the  $\text{H}\alpha$  emission, we inserted two types of fake sources into the MOSFIRE N1 spectrum in order to verify that the observed emission line is consistent with what would be predicted from the  $\text{Ly}\alpha$ . The first fake source was created by taking the integrated  $\text{Ly}\alpha$  flux within Region 2 of the LRIS slit and rescaling it to the total  $\text{H}\alpha$  flux ( $2.62 \times 10^{-17} \text{ erg cm}^{-2} \text{ s}^{-1}$ ). It was then inserted into the MOSFIRE N1 spectrum with a velocity window and spatial extent matching that of Region 2 (centred at  $-718 \text{ km s}^{-1}$ ) but centered at a spatial position away from the expected Slug emission. The results are shown in the left panel of Fig. 8, with the red rectangle denoting the fake source and the white rectangle the actual observed emission at the location of the Slug.

Since the  $\text{Ly}\alpha$  could be broadened by radiative transfer effects that would not affect the  $\text{H}\alpha$  emission, the  $\text{H}\alpha$  could be emitted with a much more concentrated velocity distribution. The second fake source, inserted into the MOSFIRE N1 spectrum at the observed  $\text{H}\alpha$  velocity centroid ( $-511 \text{ km s}^{-1}$ ), was chosen to be a 2D Gaussian with  $\sigma_{\text{vel}} = 181 \text{ km s}^{-1}$  and  $\sigma_{\text{spat}} = 18 \text{ kpc}$  and a total flux equivalent to that of the detected  $\text{H}\alpha$  flux.

As seen in the right panel of Fig. 8, the observed  $\text{H}\alpha$  emission (white rectangle) looks similar to the compact 2D Gaussian fake source (red rectangle). Though this exercise was purely for illustrative purposes, the fact that the observed emission looks similar to a reasonable expectation of the  $\text{H}\alpha$  emission supports the idea that the observed  $\text{H}\alpha$  emission is not simply due to the underlying skyline. In addition, the apparent compact size of the  $\text{H}\alpha$  as compared with the expected size seen in  $\text{Ly}\alpha$  could suggest that the  $\text{Ly}\alpha$  emission is broadened by radiative transfer effects.

### 3.4.1 The $\text{H}\alpha$ flux and the $\text{Ly}\alpha$ to $\text{H}\alpha$ ratio

We measured the  $\text{H}\alpha$  flux of the observed portion of the Slug Nebula within the MOSFIRE N1 slit using the rectangular aperture obtained as discussed above. This aperture has a spatial dimension of 81.76 kpc and spectral dimension of  $363 \text{ km s}^{-1}$  and it is spatially centred at a distance of 19.68 kpc from the intersection of the Night 1 and Night 2 slits (point ‘X’ in Fig. 1). The velocity centroid of the aperture is  $-511 \text{ km s}^{-1}$ . The region in which the  $\text{H}\alpha$  flux was measured is overplotted as a white rectangle in the top panel of Fig. 3 and both panels of Fig. 7.

We find an  $\text{H}\alpha$  flux within our aperture of  $F_{\text{H}\alpha} = 2.62 \pm 0.47 \times 10^{-17} \text{ erg cm}^{-2} \text{ s}^{-1}$  (equivalent to a surface brightness of  $\text{SB}_{\text{H}\alpha} = 2.70 \pm 0.48 \times 10^{-18} \text{ erg cm}^{-2} \text{ s}^{-1} \text{ arcsec}^{-2}$ ), where the error is calculated from the standard deviation of the fluxes in ‘pure sky’ regions as described in Section 3.3.1. Considering the  $\text{Ly}\alpha$  flux in the same spatial region obtained from the NB image (found to be  $F_{\text{Ly}\alpha} = 1.44 \pm 0.10 \times 10^{-16} \text{ erg cm}^{-2} \text{ s}^{-1}$  in Section 3.2), the  $\text{Ly}\alpha$  to  $\text{H}\alpha$  flux ratio in this region of the Slug is  $5.5 \pm 1.1$ . If, as discussed in Section 3.3.1, we take into account that the  $\text{H}\alpha$  flux might be biased high by up to  $5 \times 10^{-18} \text{ erg cm}^{-2} \text{ s}^{-1}$ , the  $\text{Ly}\alpha$  to  $\text{H}\alpha$  flux ratio would instead be around 6.9. We will discuss the possible implications of this flux ratio with respect to the physical emission mechanism and  $\text{Ly}\alpha$  escape fraction in Section 4.2.2.

### 3.5 The compact sources in the MOSFIRE data

Two line emitters were also observed in our MOSFIRE spectra. These sources were originally detected in the LRIS NB and V-band data and were dubbed compact source ‘D’ and compact source ‘C’, corresponding to the MOSFIRE N1 and MOSFIRE N2 slits, respectively. The sources are shown and labelled in Fig. 1 and their spectra are plotted in Fig. 9. Note that emitter ‘C’ is the same as source ‘C’ in Martin et al. (2015) and the compact source in our LRIS spectrum (see Fig. 2).

The bright  $\text{H}\alpha$  emission line of sources ‘C’ and ‘D’ in our MOSFIRE spectra allow us to determine the redshifts of each compact source. We find that both sources are at the same redshift of  $z \approx 2.287$ , which is slightly redshifted with respect to that of QSO A. This corresponds to a velocity offset between the compact sources and QSO A of  $\sim 355 \text{ km s}^{-1}$  that could be explained by peculiar motions within the halo of QSO A.

In addition to computing the redshifts, we also produced a  $K$ -band 1D spectrum for each source using a simple boxcar extraction. These spectra were used to calculate the  $\text{H}\alpha$  and corresponding  $\text{N II}[6583]$  line fluxes. For compact source ‘D’, we find an  $\text{H}\alpha$  flux of  $F_{\text{H}\alpha} = 6.6 \pm 0.3 \times 10^{-17} \text{ erg cm}^{-2} \text{ s}^{-1}$  and an  $\text{N II}$  flux of  $F_{\text{N II}} = 2.2 \pm 0.2 \times 10^{-17} \text{ erg cm}^{-2} \text{ s}^{-1}$ . For compact source ‘C’, we find an  $\text{H}\alpha$  flux of  $F_{\text{H}\alpha} = 4.3 \pm 0.4 \times 10^{-17} \text{ erg cm}^{-2} \text{ s}^{-1}$  and a  $\text{N II}$   $3\sigma$  flux upper-limit of  $F_{\text{N II}} = 2.4 \times 10^{-18} \text{ erg cm}^{-2} \text{ s}^{-1}$ .

## 4 DISCUSSION

In this work, we presented deep spectroscopy of the  $\text{Ly}\alpha$  and  $\text{H}\alpha$  emission of the Slug Nebula. We use these data in the following sections to discuss the physical structure of the Slug Nebula’s gas as well as the production mechanism of the Slug’s  $\text{Ly}\alpha$  emission and its implications. In Section 4.1, we use the kinematic indicators derived from the Keck I/LRIS spectroscopy (see Section 3.1) to address the question of how the Slug’s gas is physically distributed.

In Section 4.2, the Slug’s  $\text{H}\alpha$  flux, measured in Section 3.4.1, is compared to its corresponding  $\text{Ly}\alpha$  flux (Section 3.2) so as to deter-

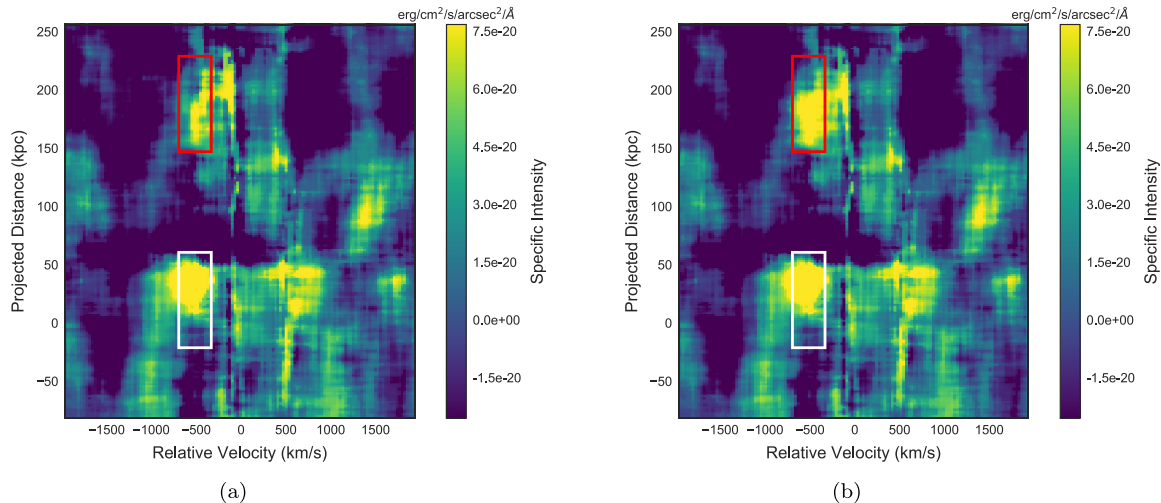


**Figure 8.** This figure presents a visual verification that our observed H $\alpha$  flux (in the white rectangle) resembles a reasonable model of the H $\alpha$  emission of the Slug. The injected fake sources represent two extremes of the possible H $\alpha$  velocity distributions: (a) the H $\alpha$  emission is assumed to have a broad velocity distribution that matches that of Region 2 in the LRIS Ly $\alpha$  spectrum (left panel) and (b) the H $\alpha$  line is assumed to have been emitted at a much more narrow range of velocities and the Ly $\alpha$  was broadened by radiative transfer effects (right panel). The left panel shows the median-smoothed image of the MOSFIRE N1 spectrum (using a kernel of 41 kpc  $\times$  363 km s $^{-1}$ ) with an injected fake source that was modelled by taking the Ly $\alpha$  flux from Region 2 in the LRIS spectrum and rescaling it to match the H $\alpha$  flux. Thus, this H $\alpha$  emission model keeps the velocity distribution of the Ly $\alpha$  emission intact and is centred at a spatial position of 188 kpc and at a velocity of  $-718$  km s $^{-1}$ . We find that the brightest region of the injected source (expected location shown as the red rectangle) appears less significant than the observed emission (in the white rectangle). Similarly, in the right panel we show the MOSFIRE N1 spectrum median-smoothed with the same kernel of 41 kpc  $\times$  363 km s $^{-1}$  that was applied in Fig. 7. The injected fake source, centred at 188 kpc and a velocity centroid that matches the observed H $\alpha$  emission, was modelled as a 2D Gaussian. The fake emission had a standard deviation in the spatial direction of 18 kpc and of 181 km s $^{-1}$  in the spectral direction and a total flux of  $2.62 \times 10^{-17}$  erg s $^{-1}$  cm $^{-2}$  that matches the observed H $\alpha$  flux. This emission model (visible within the red rectangle) better resembles the observed H $\alpha$  emission (at the location of the white rectangle), suggesting that the H $\alpha$  emission of the Slug has different kinematics than the Ly $\alpha$  and is emitted at a narrower range of velocities.

mine the emission mechanism producing the Slug’s observed Ly $\alpha$ . In particular, we distinguish between two scenarios for the production of the observed Ly $\alpha$  emission: (1) a purely *ex situ* production of QSO A that are absorbed and reemitted by neutral hydrogen in the Nebula (photon-pumping) and (2) a significant contribution of *in situ* fluorescent Ly $\alpha$  emission produced by case B recombination of the Slug’s hydrogen gas.

Finally, we examine the origin of the H $\alpha$  emission of compact sources ‘C’ and ‘D’. In Section 4.3, we use the ratio of their N II/H $\alpha$  flux to place these galaxies on a BPT diagram and determine whether these galaxies are star-forming or have a central AGN. In addition, we explore the possibility of a contribution of fluorescent emission due to QSO A.

#### 4.1 The Ly $\alpha$ kinematics of the Slug Nebula

We can gain insight into the physical structure of the gas by examining the Ly $\alpha$  kinematics. In their work, Martin et al. (2015) claimed that the brightest region of the Slug Nebula is an extended rotating hydrogen disc contained within an  $\approx 10^{13} M_{\odot}$  dark matter halo. However, the kinematics shown in Fig. 4 belie the idea that the Slug Nebula is a simple monolithic structure like a disc.

As discussed in Section 3.1, the velocity centroid as a function of spatial position (the upper left panel of Fig. 4) reveals three clearly distinguishable regions with distinct velocity centroids. These same regions are clearly recognizable in the plot of velocity dispersion as a function of spatial position and are marked by very sharp transitions at  $\sim -35$  and  $\sim 45$  kpc.

The two left-most regions comprise the Slug Nebula. The dimmer ‘Region 1’ is centred at  $\sim -50$  kpc with a characteristic velocity centroid of  $-333$  km s $^{-1}$  while the brighter ‘Region 2’ is located at  $\sim 25$  kpc with a velocity centroid of  $-555$  km s $^{-1}$ . The Ly $\alpha$  emission of the Slug is separated from that of compact source ‘C’ by a very narrow transition region ( $\sim 10$  kpc). We also see that the velocity dispersion has sharp transitions at the same locations as where we see sharp changes in the mean velocity, lending further credence to our interpretation that these are kinematically distinct regions.

Although it is difficult to disentangle velocity effects from distances along the line of sight, these sharp transitions suggest that the Slug Nebula could be composed of several structures. This is not unexpected from our theoretical understanding of cosmic structure formation: the most massive filaments of the cosmic web are composed of both diffuse material and more massive haloes containing denser gas. If the Ly $\alpha$  emission is produced by recombination radiation and therefore scales with the gas density squared, our observations would be most sensitive to detecting the densest clumps and structures within the filaments.

This interpretation of the Slug’s physical structure is inconsistent with the giant disc argued for by Martin et al. (2015), despite the fact that Martin et al.’s pseudo-slit largely overlaps with our LRIS slit. We believe that the lower spatial and spectral resolution of the pseudo-slit observations may have smoothed out the sharp transitions that we resolve, making the distribution of velocity centroids resemble that of a giant disc.

Instead, our observation reveals a very abrupt cutoff, seen in Fig. 2, of the Ly $\alpha$  flux at a spatial position of  $\sim 50$  kpc. It is currently unclear whether this sharp edge to the Ly $\alpha$  emission is due

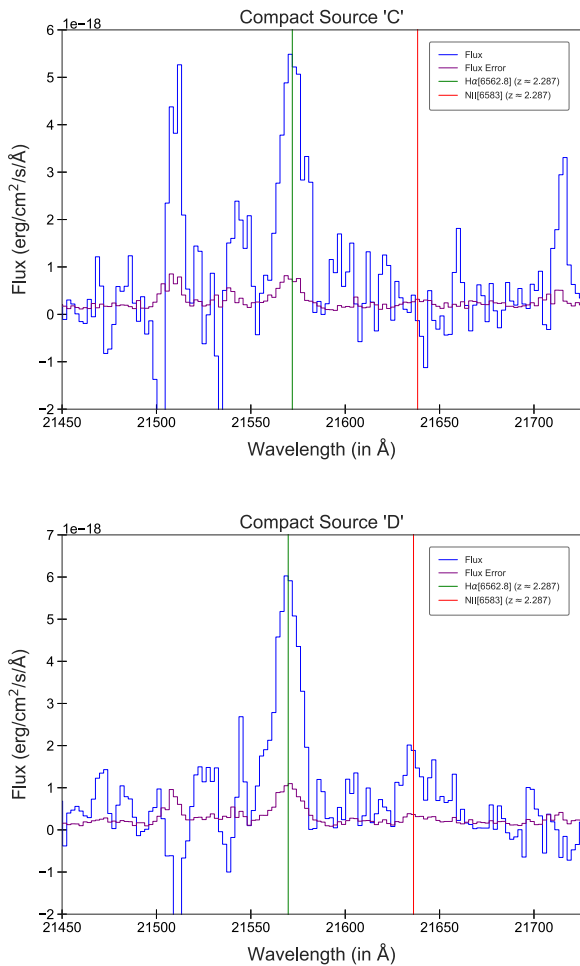


**Figure 9.** The 1D spectra of compact sources ‘C’ (top panel) and ‘D’ (bottom panel) derived from the 2D MOSFIRE N2 and N1 spectra, respectively, using a simple box extraction. The flux is shown in blue, the error array is plotted in purple, while the green and red vertical lines shows the expected wavelength of  $H\alpha$  and  $N\ II[6583]$ , respectively, given the redshift of  $z = 2.287$  for each source.

to an absence of cold gas or whether the  $Ly\alpha$  emission is instead being absorbed along the line of sight. Intriguingly, the cutoff location is very close to compact source ‘C’. However, compact source ‘C’ is located several hundred  $\text{km s}^{-1}$  on the red side of this feature and therefore we do not think that the compact source and its environment are the origin of a possible absorption feature. It is also interesting to note that the  $Ly\alpha$  emission cutoff is adjacent to the brightest region of the nebular emission. Deeper integral field observations with the Keck II/KCWI and MUSE of both  $Ly\alpha$  and other emission lines (Cantalupo et al., in preparation) could be useful to disentangle whether this may be due to a lack of quasar illumination in a particular direction (i.e. a ‘shadow’ of some absorber that is associated with the quasar) or suggestive of a possible alternative physical origin for this emission (e.g. shocks).

## 4.2 Constraining the emission mechanism of the Slug Nebula

Cantalupo et al. (2014) presents two possible mechanisms that could power the  $Ly\alpha$  emission of the Slug Nebula. In the first case, Lyman continuum photons produced by the nearby QSO A ionize the gas of the Nebula, producing  $Ly\alpha$  photons as the hydrogen atoms

recombine. In the so-called ‘case A’, the gas is optically thin to ionizing radiation, while the opposite optically-thick situation is referred to as ‘case B’. In the absence of dust, for reasonable nebular temperatures of  $5 \times 10^3 - 2 \times 10^4$  K and electron densities  $n_e < 10^4 \text{ cm}^{-3}$  the expected integrated  $Ly\alpha/H\alpha$  ratio for case B recombination should range between 8.1 and 11.6 (Hummer & Storey 1987). In order to remain consistent with the broader literature, we use the conventional case B ratio of 8.7 set by Hu, Cowie & McMahon (1998) (for further discussion, see Hayes 2015; Henry et al. 2015; Trainor et al. 2015).

Note that this ratio assumes spatially integrated measurements with apertures large enough to capture the full  $Ly\alpha$  flux as the  $Ly\alpha$  can scatter and spatially diffuse while  $H\alpha$  cannot. If the spatial aperture does not encompass all the  $Ly\alpha$ , the measured  $Ly\alpha/H\alpha$  may be considered to be a lower limit to the true value.

In the second case, the  $Ly\alpha$  emission is produced as mostly neutral hydrogen gas absorbs scattered  $Ly\alpha$  and doppler-shifted Balmer continuum photons (‘photon-pumping’) from the broad-line region of QSO A and re-emits them as  $Ly\alpha$  photons into our line of sight. In this scenario, we would expect little to no  $H\alpha$  to be produced. Thus, we would expect to only obtain an upper limit on  $H\alpha$ , and therefore a lower limit on the  $Ly\alpha/H\alpha$  ratio. If we were to observe a  $Ly\alpha/H\alpha$  ratio of at least 12 or so, this scenario could then be distinguished from the recombination case.

### 4.2.1 Evidence for a detection of the Slug Nebula’s $H\alpha$ emission

In order to differentiate between these two production mechanisms, it is important to ensure that our  $H\alpha$  detection in the MOSFIRE N1 spectrum originated from the Slug Nebula. As mentioned in Section 3.4, despite of the presence of a bright, imperfectly subtracted skyline at the location of our  $H\alpha$  detection there are several points that help support the idea that the measured  $H\alpha$  flux is indeed emission from the Slug.

(i) *There is a significant  $H\alpha$  emission:* The  $H\alpha$  flux we measured corresponds to a  $5.6\sigma$  detection if we use our empirical sky-noise estimator. If we instead use the error file from the MOSFIRE DRP to estimate the noise, the SNR doubles. In either case, the detection is significant despite being on top of a skyline. Though the  $H\alpha$  flux we measure is not clearly visible in the unsmoothed 2D MOSFIRE spectrum shown in Fig. 3, once the spectrum is smoothed, as shown in Fig. 7, the emission line becomes evident.

(ii) *The  $H\alpha$  emission is located where it is expected:* When determining the aperture in which to measure the  $H\alpha$  flux, we determined the spatial centroid and width solely from the NB image. It is therefore notable that the only significant emission besides QSO A and compact source ‘D’ in the region is located within these independently derived spatial constraints. In addition, it is striking that despite our priorless search for the velocity centroid of the  $H\alpha$  emission, it coincides so well with the velocity centroid of the  $Ly\alpha$  emission that we derived from the LRIS slit kinematics.

Note that while the LRIS slit does not match the orientation of the MOSFIRE N1 slit, they do have an overlap region at point ‘X’, where the velocity centroids of the  $Ly\alpha$  and  $H\alpha$  are very closely matched. In addition, the LRIS kinematics shown in Fig. 4 indicate a constant velocity centroid within each region. Since the MOSFIRE N1 slit goes squarely through Region 2 of the Nebula, it is unlikely that the  $Ly\alpha$  velocity centroid within a MOSFIRE N1-like slit would differ much from our observed LRIS kinematics.

(iii) *The  $H\alpha$  emission looks like what we would expect from the  $Ly\alpha$ :* In order to verify that our observed  $H\alpha$  emission looked

reasonably similar to what we would expect from the Slug Nebula, we visually compared it to two simple emission prediction models based on the LRIS Ly $\alpha$  emission and an assumption of case B recombination radiation.

As described in Section 3.4 and shown in Fig. 8, we found that our observed H $\alpha$  detection is visually consistent with a compact 2D Gaussian emission model ( $\sigma_{\text{vel}} = 181 \text{ km s}^{-1}$  and  $\sigma_{\text{spat}} = 18 \text{ kpc}$ ) with a total flux that is the same as our observed H $\alpha$  flux.

Thus, there is significant H $\alpha$  emission at a location consistent with that of the Ly $\alpha$  emission of the Slug Nebula and that it looks similar to what would be expected assuming a relatively narrow H $\alpha$  velocity distribution produced by case B recombination radiation. These facts together indicate that our MOSFIRE H $\alpha$  flux is very likely a true detection of the Slug Nebula’s H $\alpha$  emission. However, the only way to definitively confirm the H $\alpha$  detection at much higher significance level would require observations that are not affected by skylines, i.e. from space using the *James Webb Space Telescope* (JWST).

#### 4.2.2 The fluorescent nature of the Slug Nebula’s emission

The ratio of the Ly $\alpha$  flux, measured in Section 3.2, to the corresponding H $\alpha$  flux, calculated in Section 3.4.1, allows us to determine which mechanism is primarily responsible for powering the Slug Nebula’s emission. We find a ratio of

$$\frac{F_{\text{Ly}\alpha}}{F_{\text{H}\alpha}} = 5.5 \pm 1.1. \quad (3)$$

Despite the large uncertainties and the limitations of our current observations, our measured value of  $F_{\text{Ly}\alpha}/F_{\text{H}\alpha}$  is clearly much lower than the ratio of  $F_{\text{Ly}\alpha}/F_{\text{H}\alpha} > 12$  expected if the Ly $\alpha$  emission of the Slug Nebula were primarily being produced via scattering of the quasar broad-line region. Rather, it is remarkably close to the ‘standard’ case B recombination ratio of 8.7. If, as discussed in Section 3.3.1 and Section 3.4.1, the H $\alpha$  flux is biased slightly high due to our aperture selection, the flux ratio could be as large as  $F_{\text{Ly}\alpha}/F_{\text{H}\alpha} = 6.9 \pm 1.1$ , driving it even closer to the canonical 8.7 value. Observing Ly $\alpha$  to H $\alpha$  emission ratios that are so close to those expected for case B recombination implies that the gas in the Slug Nebula must be mostly ionized, presumably by QSO A, optically thick to Ly $\alpha$  photons, and producing the fluorescent Ly $\alpha$  and corresponding H $\alpha$  emission *in situ* as the gas recombines. Of course, some small contribution due to photon-pumping from the quasar broad-line region cannot be excluded.

In studies of Ly $\alpha$  emitting galaxies, it is customary to interpret this ratio in terms of the Ly $\alpha$  escape fraction ( $f_{\text{esc}}$ ). The Ly $\alpha$  escape fraction compares the ratio of observed  $F_{\text{Ly}\alpha}/F_{\text{H}\alpha}$  (where  $F_{\text{H}\alpha}$  is generally dust corrected) to the ideal case B recombination value of 8.7 (see i.e. equation 2 of Atek et al. 2009). If we convert our measurement of the  $F_{\text{Ly}\alpha}/F_{\text{H}\alpha}$  ratio from equation (3) into a Ly $\alpha$  escape fraction, it would correspond to  $f_{\text{esc}} \sim 63$  per cent. This value is in keeping with the escape fractions found for Ly $\alpha$ -selected galaxies at redshifts of  $z \sim 2\text{--}3$ , which range from a few per cent to over 100 per cent, but are typically  $\sim 30$  per cent (e.g. Hayes et al. 2010; Steidel et al. 2011; Erb et al. 2014; Trainor et al. 2015; Matthee et al. 2016). The presence of dust is often used to explain escape fractions that are below 100 per cent, since dust preferentially destroys Ly $\alpha$  as compared to H $\alpha$ . Hayes et al. (2010); Steidel et al. (2011), and to a lesser extent Matthee et al. (2016), all observe that  $f_{\text{esc}}$  is anti-correlated with dust attenuation.

However, it is important to remember that the Slug Nebula is not a Ly $\alpha$  galaxy. Rather, it is a very massive reservoir of cool gas that spans over 450 kpc, has no detected stellar continuum component, and as discussed in Section 4.1, has kinematics that are inconsistent with being a massive rotating disc. Therefore, as discussed in Cantalupo et al. (2014), the Slug Nebula is likely a filamentary structure in the IGM, and we do not expect significant amounts of dust to be present on these intergalactic scales. Indeed, the non-detection of metal emission, from C IV[1549] (Arrigoni Battaia et al. 2015b) suggests that the metallicity of the Slug is not as high as in the ISM of high-redshift galaxies.

Another explanation for the  $f_{\text{esc}} < 100$  per cent observed in Ly $\alpha$  emitting galaxies was proposed by Steidel et al. (2011). As they point out, it is not necessary to destroy Ly $\alpha$  photons to affect the Ly $\alpha$  flux measurement. Resonant scattering causes the Ly $\alpha$  photons to diffuse spatially outwards while leaving the non-resonant H $\alpha$  unaffected. Therefore, an aperture that encompasses all of the H $\alpha$  emission will likely be missing a significant amount of the Ly $\alpha$ , leading to measured escape fractions that are less than 100 per cent.

This scattering of Ly $\alpha$  photons to larger spatial scales is probably the dominant effect contributing to why our measured Ly $\alpha$  flux is below what we would expect for case B recombination. We measure the Ly $\alpha$  flux corresponding to the MOSFIRE N1 slit by integrating the Ly $\alpha$  flux within a pseudo-slit region of the NB image. We are therefore likely missing a significant fraction of the Ly $\alpha$  photons produced in this bright region, particularly those that are scattered by more than the 1 arcsec slit width. This explanation is further supported by the fact that we see possible radiative transfer effects playing a role in producing a Ly $\alpha$  spectral width that is broadened compared to that of the H $\alpha$ . In this case, we would expect higher Ly $\alpha$  to H $\alpha$  ratios in the outer, fainter regions of the Slug Nebula that are currently not covered by our spectroscopic slit, which was centred on the brightest emission. Deep H $\alpha$  NB or integral field spectroscopic observations would be needed to confirm this scenario.

As discussed in Borisova et al. (2016), another conceivable contribution to the lower than expected Ly $\alpha$  flux could be ‘filter-loss’ effects. These filter-losses occur when a portion of the broad Ly $\alpha$  emission falls outside of the peak transmission of the NB filter. In order to determine whether filter-losses could significantly affect our measured Ly $\alpha$ /H $\alpha$  ratio, we compared the laboratory-measured NB filter transmission curve to the Ly $\alpha$  kinematics from our LRIS spectrum (assuming that these kinematics are similar to those that would have been observed using an LRIS slit that matched the MOSFIRE N1 slit). We find that the Ly $\alpha$  emission coincides well with the NB filter peak transmission and that any filter-losses would be too small to explain the lower than expected Ly $\alpha$  to H $\alpha$  ratio.

The recombination nature of the Slug Nebula’s emission has important implications for the conditions of the gas on intergalactic and circumgalactic scales around quasars. As discussed in detail in Cantalupo et al. (2014) and Arrigoni Battaia et al. (2015b) (also see Cantalupo 2017 for a review), the large Ly $\alpha$  (and H $\alpha$ ) SB of the Slug in the recombination case would imply very high gas densities ( $n > 1 \text{ cm}^{-3}$ ) that can only be explained by large clumping factors ( $C \sim 1000$ ), and therefore small volume filling factors, given the large intergalactic scales associated with the emission. In addition, there are indications that the Ly $\alpha$  is being broadened due to radiative transfer effects. This suggests that the gas is highly ionized but not completely optically thin to the Ly $\alpha$  radiation produced by recombination. This would imply a neutral hydrogen column den-

sity significantly above  $10^{14} \text{ cm}^{-2}$  and will help future studies to further constrain the ionization parameter, total column densities, and volume densities of the gas.

### 4.3 Elucidating the nature of compact sources ‘C’ and ‘D’

In Section 3.5, we calculated the  $H\alpha$  and  $N\text{II}[6583]$  fluxes for compact sources ‘C’ and ‘D’, which we can use to surmise the origin of the  $H\alpha$  emission. Cantalupo et al. (in preparation) modelled the UV continuum emission of compact source ‘C’ using `STARBUST99` (Leitherer et al. 1999) and found that the galaxy was consistent with having little to no dust and a star formation rate (SFR) of  $\approx 2\text{--}3 M_{\odot} \text{ yr}^{-1}$ . We can convert this SFR into a predicted  $H\alpha$  flux by using the classic conversion of SFR to  $H\alpha$  luminosity from Kennicutt (1998). In this way, we calculate that a SFR =  $3 M_{\odot} \text{ yr}^{-1}$  corresponds to an expected  $H\alpha$  flux of  $F_{H\alpha, \text{expected}} = 9.0 \times 10^{-18} \text{ erg cm}^{-2} \text{ s}^{-1}$ . Comparing this expected flux to the observed  $H\alpha$  flux measured in Section 3.5, we find that the observed flux is 4.8 times higher than what would be predicted from star formation alone when using the Kennicutt (1998) relation.

We can perform a similar analysis on compact source ‘D’. Since we do not have a UV spectrum of compact source ‘D’, we cannot do the full modelling of its UV continuum emission, as we did for compact source ‘C’. Instead, we can attempt to rescale the SFR we computed for compact source ‘C’ to one for compact source ‘D’ by comparing their UV continuum fluxes as determined from the V-band photometry (see Fig. 1). We find that  $F_{UV, C}/F_{UV, D} \approx 2.9$ , suggesting a SFR for compact source ‘D’ of  $\sim 1 M_{\odot} \text{ yr}^{-1}$ . It is important to note, however, that this method implicitly assumes that compact source ‘D’, like ‘C’, has little to no dust extinction in the UV continuum. A SFR of  $1 M_{\odot} \text{ yr}^{-1}$  corresponds to a predicted  $H\alpha$  flux of  $F_{H\alpha, \text{expected}} = 3.0 \times 10^{-18} \text{ erg cm}^{-2} \text{ s}^{-1}$  for compact source ‘D’, which, as in the case of compact source ‘C’, is a factor of  $F_{H\alpha, \text{observed}}/F_{H\alpha, \text{expected}} = 22$  times lower than the observed  $H\alpha$  flux.

Both of these comparisons rely on the classic Kennicutt (1998) value based on the typical conditions of star-formation in nearby, massive galaxies. However, interpreting the additional  $H\alpha$  flux as evidence of a contribution of ionizing radiation from a source other than star-formation is not a secure conclusion for many low-mass and vigorously star-forming galaxies. A classic method of interpreting the ionization state of a galaxy is the N2-BPT diagram (Baldwin, Phillips & Terlevich 1981; Veilleux & Osterbrock 1987) which compares the ratio of  $N\text{II}/H\alpha$  to  $O\text{III}/H\beta$ . When examining this relation for low-redshift systems, Brinchmann, Pettini & Charlot (2008a); Brinchmann, Kunth & Durret (2008b) find a tail of star-forming systems with small  $N\text{II}/H\alpha$  and high  $O\text{III}/H\beta$ , generally with high specific SFRs ( $10^7\text{--}10^8 \text{ yr}^{-1}$ .) Such galaxies are common in surveys of star-forming systems at  $z \sim 2$ , yielding a N2-BPT diagram populated with extreme ratios of  $N\text{II}/H\alpha$  (Maseda et al. 2013; Nakajima et al. 2013; Steidel et al. 2014; Shapley et al. 2015; Holden et al. 2016; Trainor et al. 2016; Strom et al. 2017).

To produce these extreme ratios requires a much harder ionizing flux than typically produced by star-forming regions in, for example, the Milky Way. One method of producing such ratios would be the nearby QSO A, but the frequency of these galaxies outside of the neighbourhoods of QSOs points to different conditions of star-formation such as is discussed in, for instance, Kewley et al. (2013), Steidel et al. (2016), and Eldridge et al. (2017).

## 5 CONCLUSIONS

The recent discovery of ELANe (also referred to as giant  $\text{Ly}\alpha$  nebulae) around quasars has opened up a new observational window into the study of intergalactic gas in emission on scales of several hundred kpc around massive galaxies at high redshift (see e.g. Cantalupo 2017 for a review). The Slug Nebula is one of the largest and most luminous among the ELANe discovered to date. Its very high  $\text{Ly}\alpha$  surface brightness extends over 450 physical kpc around the bright quasar UM287 at  $z = 2.283$  (Cantalupo et al. 2014).

Depending on the  $\text{Ly}\alpha$  emission mechanism, these high SB values would imply either a ‘clumpy’ and mostly ionized medium (in the case of recombination radiation) or large column densities of neutral gas (in the case of scattering radiation from the quasar broad-line emission region), as discussed in Cantalupo et al. (2014).

In order to clearly distinguish between these two scenarios, we searched for the non-resonant hydrogen  $H\alpha$  emission from the brightest part of the Slug Nebula by means of deep Keck I/MOSFIRE long-slit spectroscopic observations. In addition, we obtained a deep, moderately high-resolution  $\text{Ly}\alpha$  Keck I/LRIS spectrum in order to guide our  $H\alpha$  emission search in the spectral direction and to study the detailed kinematics of the Slug.

(i) Compared to previous lower resolution and lower signal-to-noise  $\text{Ly}\alpha$  spectral studies, our LRIS observation of  $\text{Ly}\alpha$  emission revealed a more complex kinematic pattern than that of a simple, giant rotating disc (Martin et al. 2015). Instead, as presented in Section 3.1 and discussed in Section 4.1, these kinematics seem more consistent with the presence of at least two structures that are clearly separated in velocity space.

(ii) We then independently analysed the  $H\alpha$  spectrum obtained using Keck I/MOSFIRE. By optimizing the spectral aperture size and velocity centroid using a curve-of-growth approach, we found an  $H\alpha$  detection of  $F_{H\alpha} = 2.62 \pm 0.47 \times 10^{-17} \text{ erg cm}^{-2} \text{ s}^{-1}$  with a significance of  $\sim 5.6\sigma$ , at a velocity of  $-511 \text{ km s}^{-1}$  from the systemic redshift of the UM287 quasar ( $z = 2.283$ ) (see Section 3.3 for more details). Such a detection is exactly at the spatial position obtained from the LRIS NB image and extremely close to the velocity expected from the  $\text{Ly}\alpha$  kinematics derived from the LRIS spectrum. This reinforces the reliability of the detected emission.

(iii) The observed  $H\alpha$  signal overlaps with residuals from a relatively bright NIR skyline, reducing the overall signal-to-noise ratio and hampering the possibility of a detailed kinematic analysis of this emission line. However, our curve-of-growth analysis in Section 3.3.1 suggests that the  $H\alpha$  emission could be significantly more narrow ( $181 \text{ km s}^{-1}$ ) than its  $\text{Ly}\alpha$  counterpart ( $418 \text{ km s}^{-1}$ ). This possible broadening of the  $\text{Ly}\alpha$  emission as compared to the  $H\alpha$  emission would naturally be produced by resonant scattering of  $\text{Ly}\alpha$  photons if the Nebula were optically thick to the  $\text{Ly}\alpha$  radiation, thus implying  $N_{\text{HI}} > 10^{14} \text{ cm}^{-2}$ .

(iv) The most important result from our observations is the direct measurement of the  $\text{Ly}\alpha$  to  $H\alpha$  ratio in the region covered by our MOSFIRE N1 slit. We found the ratio  $F_{\text{Ly}\alpha}/F_{H\alpha}$  to be  $5.5 \pm 1.1 +1.4$  (sys), see Section 3.3.1 for a discussion of the systematic error. Since photon-pumping (scattering emission) from the quasar broad-line region contributes  $\text{Ly}\alpha$  photons without producing any corresponding  $H\alpha$  photons in the Nebula, we would expect this type of emission mechanism to result in very high values of  $F_{\text{Ly}\alpha}/F_{H\alpha}$  that would be well above the expected case B recombination (8.7 for total integrated emission or slightly lower for a slit observation like our own).

Therefore, the fact that the observed  $\text{Ly}\alpha$  to  $H\alpha$  is this close to the expected case B recombination value suggests that any contribu-

tion to the  $\text{Ly}\alpha$  emission from these alternate emission mechanisms should be negligible and that the dominant source of  $\text{Ly}\alpha$  emission for the Slug Nebula is recombination radiation. As derived in Cantalupo et al. (2014),  $\text{H I}$  column densities above  $N_{\text{HI}} \sim 10^{19} \text{ cm}^{-2}$  are expected to have a significant  $\text{Ly}\alpha$  flux contribution due to scattering from the quasar broad-line region. Thus, our  $\text{Ly}\alpha$  to  $H\alpha$  flux ratio places an upper limit on the  $\text{H I}$  column density of  $N_{\text{HI}} < 10^{19} \text{ cm}^{-2}$ .

Taken as a whole, the above conclusions imply that the  $\text{Ly}\alpha$  emission from the Slug Nebula is powered by case B recombination with minimal contributions from the scattering of *ex situ*  $\text{Ly}\alpha$  photons. Thus, the IGM and CGM around UM287 must be highly ionized, with an  $\text{H I}$  column density between  $10^{14}$  and  $10^{19} \text{ cm}^{-2}$ . Considering the work of Cantalupo et al. (2014) and Arrigoni Battaia et al. (2015b), this suggests that the observed Slug Nebula emission requires the presence of high-density gas structures (clumps) with a small volume filling factor. Though the exact gas-density distribution is not well constrained, these clumps could be the high-density tail of a very broad gas distribution (Cantalupo et al, in preparation).

Despite the technical challenges and limitations of extended, faint emission spectroscopy in the NIR, our results demonstrate the potential of  $H\alpha$  intergalactic fluorescent observations at high redshift. Future surveys from space-based observatories such as *JWST* that do not suffer from the presence of skylines would be necessary for a significant step forward in the  $H\alpha$  study of the Slug Nebula and for other enormous  $\text{Ly}\alpha$  nebulae at high redshift.

## ACKNOWLEDGEMENTS

The authors would like to thank the referee for their incredibly helpful and thoughtful review of this paper. The National Science Foundation (NSF) grants AST-1010004 and AST-1412981 helped support CNL, SC, and Jason Prochaska, who participated in the data collection, reduction, and analysis. SC gratefully acknowledges support from Swiss National Science Foundation grant PP00P2\_163824. Support for this work was also provided by the National Aeronautics and Space Administration (NASA) through grant *HST*-AR-13904.001-A (PM) and the National Science Foundation Graduate Research Fellowship under Grant No. NSF DGE1339067 (CNL). PM also acknowledges a NASA contract supporting the Wide Field Infra-Red Survey Telescope EXtragalactic Potential Observations Science Investigation Team (15-WFIRST15-0004), administered by Goddard Space Flight Center, and thanks the Préfecture of the Ile-de-France Region for the award of a Blaise Pascal International Research Chair, managed by the Fondation de l'Ecole Normale Supérieure. The data presented herein were obtained at the W. M. Keck Observatory, which is operated as a scientific partnership among the California Institute of Technology, the University of California and the National Aeronautics and Space Administration. The Observatory was made possible by the generous financial support of the W. M. Keck Foundation. The authors wish to recognize and acknowledge the very significant cultural role and reverence that the summit of Mauna Kea has always had within the indigenous Hawaiian community. We are most fortunate to have the opportunity to conduct observations from this mountain.

## REFERENCES

- Arrigoni Battaia F., Hennawi J. F., Prochaska J. X., Cantalupo S., 2015b, *ApJ*, 809, 163
- Arrigoni Battaia F., Prochaska J. X., Hennawi J. F., Obreja A., Buck T., Cantalupo S., Dutton A. A., Macciò A. V., 2018, *MNRAS*, 473, 3907
- Arrigoni Battaia F., Yang Y., Hennawi J. F., Prochaska J. X., Matsuda Y., Yamada T., Hayashino T., 2015a, *ApJ*, 804, 26
- Astropy Collaboration, 2013, *A&A*, 558, A33
- Atek H., Kunth D., Schaerer D., Hayes M., Deharveng J. M., Östlin G., Mas-Hesse J. M., 2009, *A&A*, 506, L1
- Baldwin J. A., Phillips M. M., Terlevich R., 1981, *PASP*, 93, 5
- Bohlin R. C., 2014, *AJ*, 147, 127
- Borisova E. et al., 2016, *ApJ*, 831, 39
- Brinchmann J., Kunth D., Durret F., 2008b, *A&A*, 485, 657
- Brinchmann J., Pettini M., Charlot S., 2008a, *MNRAS*, 385, 769
- Cai Z., et al., 2017, *ApJ*, 837, 71
- Cai Z., et al., 2018, *ApJ*, 861, L3
- Cantalupo S., 2017, in Fox A., Davè R., eds, *Astrophysics and Space Science Library* Vol. 430, *Astrophysics and Space Science Library*. p. 195
- Cantalupo S., Arrigoni-Battaia F., Prochaska J. X., Hennawi J. F., Madau P., 2014, *Nature*, 506, 63
- Cantalupo S., Porciani C., Lilly S. J., Miniati F., 2005, *ApJ*, 628, 61
- Chapman S. C., Lewis G. F., Scott D., Richards E., Borys C., Steidel C. C., Adelberger K. L., Shapley A. E., 2001, *ApJ*, 548, L17
- da Ângela J. et al., 2008, *MNRAS*, 383, 565
- Dekel A. et al., 2009, *Nature*, 457, 451
- Dey A. et al., 2005, *ApJ*, 629, 654
- Eldridge J. J., Stanway E. R., Xiao L., McClelland L. A. S., Taylor G., Ng M., Greis S. M. L., Bray J. C., 2017, *PASA*, 34, e058
- Erb D. K. et al., 2014, *ApJ*, 795, 33
- Fumagalli M. et al., 2017, *MNRAS*, 471, 3686
- Gallego S. G. et al., 2018, *MNRAS*, 475, 3854
- Geach J. E. et al., 2009, *ApJ*, 700, 1
- Hayes M., 2015, *PASA*, 32, e027
- Hayes M. et al., 2010, *Nature*, 464, 562
- Hennawi J. F., Prochaska J. X., Cantalupo S., Arrigoni-Battaia F., 2015, *Science*, 348, 779
- Henry A., Scarlata C., Martin C. L., Erb D., 2015, *ApJ*, 809, 19
- Hine N. K. et al., 2016, *MNRAS*, 460, 4075
- Holden B. P. et al., 2016, *ApJ*, 820, 73
- Hu E. M., Cowie L. L., McMahon R. G., 1998, *ApJ*, 502, L99
- Hummer D. G., Storey P. J., 1987, *MNRAS*, 224, 801
- Hunter J. D., 2007, *Comput. Sci. Eng.*, 9, 90
- Jones E. et al., 2001, SciPy: Open source scientific tools for Python, Available at: <http://www.scipy.org/>
- Kennicutt R. C., Jr., 1998, *ARA&A*, 36, 189
- Kewley L. J., Maier C., Yabe K., Ohta K., Akiyama M., Dopita M. A., Yuan T., 2013, *ApJ*, 774, L10
- Kriek M. et al., 2015, *ApJS*, 218, 15
- Leitherer C. et al., 1999, *ApJS*, 123, 3
- Mandelker N., Padnos D., Dekel A., Birnboim Y., Burkert A., Krumholz M. R., Steinberg E., 2016, *MNRAS*, 463, 3921
- Marino R. A. et al., 2018, *ApJ*, 859, 53
- Martin D. C., Matuszewski M., Morrissey P., Neill J. D., Moore A., Cantalupo S., Prochaska J. X., Chang D., 2015, *Nature*, 524, 192
- Maseda M. V. et al., 2013, *ApJ*, 778, L22
- Matsuda Y. et al., 2004, *AJ*, 128, 569
- Matthee J., Sobral D., Oteo I., Best P., Smail I., Röttgering H., Paulino-Afonso A., 2016, *MNRAS*, 458, 449
- McLean I. S. et al., 2010, in McLean I. S., Ramsay S. K., Takami H., eds, *Ground-based and Airborne Instrumentation for Astronomy III (SPIE Proceedings Vol. 7735)*. SPIE Press, Bellingham, p. 77351E
- McLean I. S. et al., 2012, in McLean I. S., Ramsay S. K., Takami H., eds, *Ground-based and Airborne Instrumentation for Astronomy IV*. SPIE Press, Bellingham, p. 84460J
- Miley G., De Breuck C., 2008, *A&A Rev.*, 15, 67
- Nakajima K., Ouchi M., Shimasaku K., Hashimoto T., Ono Y., Lee J. C., 2013, *ApJ*, 769, 3
- Nelson D., Vogelsberger M., Genel S., Sijacki D., Kereš D., Springel V., Hernquist L., 2013, *MNRAS*, 429, 3353
- Oke J. B. et al., 1995, *PASP*, 107, 375
- Overzier R. A., Nesvadba N. P. H., Dijkstra M., Hatch N. A., Lehnert M. D., Villar-Martín M., Wilman R. J., Zirm A. W., 2013, *ApJ*, 771, 89

- Perez F., Granger B. E., 2007, *Comput. Sci. Eng.*, 9, 21
- Prescott M. K. M., Dey A., Jannuzi B. T., 2009, *ApJ*, 702, 554
- Prescott M. K. M., Martin C. L., Dey A., 2015a, *ApJ*, 799, 62
- Prescott M. K. M., Momcheva I., Brammer G. B., Fynbo J. P. U., Møller P., 2015b, *ApJ*, 802, 32
- Prochaska J. F., Hennawai J., Burles S., 2017, XIDL, Available at: <https://github.com/profxj/xidl>
- Prochaska J. X. et al., 2013, *ApJ*, 776, 136
- Pych W., 2004, *PASP*, 116, 148
- Pych W., 2012, dcr: Cosmic Ray Removal, Astrophysics Source Code Library, record ascl:1207.006
- Shapley A. E. et al., 2015, *ApJ*, 801, 88
- Steidel C. C., Adelberger K. L., Shapley A. E., Pettini M., Dickinson M., Giavalisco M., 2000, *ApJ*, 532, 170
- Steidel C. C., Bogosavljević M., Shapley A. E., Kollmeier J. A., Reddy N. A., Erb D. K., Pettini M., 2011, *ApJ*, 736, 160
- Steidel C. C., Strom A. L., Pettini M., Rudie G. C., Reddy N. A., Trainor R. F., 2016, *ApJ*, 826, 159
- Steidel C. C. et al., 2014, *ApJ*, 795, 165
- Strom A. L., Steidel C. C., Rudie G. C., Trainor R. F., Pettini M., Reddy N. A., 2017, *ApJ*, 836, 164
- Trainor R. F., Steidel C. C., 2012, *ApJ*, 752, 39
- Trainor R. F., Steidel C. C., Strom A. L., Rudie G. C., 2015, *ApJ*, 809, 89
- Trainor R. F., Strom A. L., Steidel C. C., Rudie G. C., 2016, *ApJ*, 832, 171
- Veilleux S., Osterbrock D. E., 1987, *ApJS*, 63, 295
- Villar-Martín M., 2007, *New Astron. Rev.*, 51, 194
- Voit G. M., Bryan G. L., O’Shea B. W., Donahue M., 2015, *ApJ*, 808, L30
- Walt S. v. d., Colbert S. C., Varoquaux G., 2011, *Comput. Sci. Eng.*, 13, 22
- Yang Y., Zabludoff A., Jahnke K., Davé R., 2014, *ApJ*, 793, 114
- Yang Y., Zabludoff A., Tremonti C., Eisenstein D., Davé R., 2009, *ApJ*, 693, 1579

This paper has been typeset from a  $\text{\TeX}/\text{\LaTeX}$  file prepared by the author.